DARCLOS: a cloud shadow detection algorithm for TROPOMI

Victor J. H. Trees [1,2], Ping Wang [1], Piet Stammes [1], Lieuwe G. Tilstra [1], David P. Donovan [1,2], and A. Pier Siebesma [1,2]

[1]Royal Netherlands Meteorological Institute (KNMI), De Bilt, the Netherlands
[2]Delft University of Technology, Delft, the Netherlands

Correspondence: Victor Trees (victor.trees@knmi.nl)

Abstract. Cloud shadows are observed by the TROPOMI satellite instrument as a result of its high spatial resolution as compared to its predecessor instruments. These shadows contaminate TROPOMI's air quality measurements, because shadows are generally not taken into account in the models that are used for aerosol and trace gas retrievals. If the shadows are to be removed from the data, or if shadows are to be studied, an automatic detection of the shadow pixels is needed. We present the Detection AlgoRithm for CLOud Shadows (DARCLOS) for TROPOMI, which is the first cloud shadow detection algorithm for a spaceborne spectrometer. DARCLOS raises potential cloud shadow flags (PCSFs), actual cloud shadow flags (ACSFs) and spectral cloud shadow flags (SCSFs). The PCSFs indicate the TROPOMI ground pixels that are potentially affected by cloud shadows based on a geometric consideration with safety margins. The ACSFs are a refinement of the PCSFs using spectral reflectance information of the PCSF pixels, and identify the TROPOMI ground pixels that are confidently affected by cloud shadows. Because we find indications of the wavelength dependence of cloud shadow extents in the UV, the SCSF is a wavelength dependent alternative for the ACSF at the wavelengths of TROPOMI's air quality retrievals. We validate the PCSF and ACSF with true color images made by the VIIRS instrument on board of Suomi NPP orbiting in close proximity to TROPOMI on board of Sentinel-5P. We find that the cloud evolution during the overpass time difference between TROPOMI and VIIRS complicates this validation strategy, implicating that an alternative cloud shadow detection approach using co-located VIIRS observations could be problematic. We conclude that the PCSF can be used to exclude cloud shadow contamination from TROPOMI data, while the ACSF and SCSF can be used to select pixels for the scientific analysis of cloud shadow effects.

1 Introduction

Air quality monitoring from space using satellite spectrometers started in 1978 with the launch of the first Total Ozone Mapping Spectrometer (TOMS) instrument on board the Nimbus-7 satellite. TOMS globally measured aerosol properties and concentrations of O_3 and SO_2 in the Earth's atmosphere on a daily basis, retrieved from the Earth's reflectance of sunlight using six ultraviolet (UV) wavelength bands (Heath et al., 1975). The first high-spectral resolution spectrometer was the Global Ozone Monitoring Experiment (GOME) (Burrows et al., 1999) launched in 1995, followed by the SCanning Imaging Absorption spectroMeter for Atmospheric ChartograpHY (SCIAMACHY) (Bovensmann et al., 1999), the Ozone Monitoring Instrument (OMI) (Levelt et al., 2006), the GOME-2 A/B/C instruments (Munro et al., 2016) and, most recently, the TROPOspheric Mon-

itoring Instrument (TROPOMI) (Veefkind et al., 2012), allowing for trace gas retrieval using differential absorption features in the spectra of the Earth's reflectance (Platt and Stutz, 2008).

The spatial resolutions of TOMS, GOME, SCIAMACHY, OMI and GOME-2 have been 50×50 km^2, 320×40 km^2, 60×30 km^2, 24×13 km^2 and 80×40 km^2, respectively. Those resolutions are too coarse to discern kilometer-scale clouds or cloud shadows. The pixels of those spectrometers often have been partly cloudy, such that the effects of clouds, cloud shadows and cloud-free regions are blended. Because of the inability to distinguish between those effects and the complexity of three-dimensional (3-D) radiative transfer, state-of-art algorithms for satellite spectrometers employ one-dimensional (1-D) radiative transfer models, which neglect 3-D cloud effects on cloud-free regions inside the partly cloudy pixels or on adjacent cloud-free pixels. For example, the FRESCO (Fast REtrieval Scheme for Clouds from the Oxygen A band) cloud retrieval algorithm uses the independent pixel approximation, and does not take into account cloud shadows (Koelemeijer et al., 2001; Wang et al., 2008). However, although cloud shadows are hardly visible on the coarse resolution measurement grids of those spectrometers, they do in principle contaminate the total radiances of the large pixels.

TROPOMI on board of the ESA Sentinel-5P satellite was launched in October 2017 and is the spaceborne spectrometer with the highest spatial resolution to date: the ground pixels have dimensions of 7.2×3.6 km^2 in the nadir viewing direction, and decreased to 5.6×3.6 km^2 on 6 August 2019.[1] TROPOMI provides daily global maps of aerosol properties and concentrations of O_3, NO_2, SO_2 and HCHO from ultraviolet-visible (UV–VIS, 267–499 nm) wavelengths, of cloud properties from near-infrared (NIR, 661–786 nm) wavelengths and concentrations of CO and CH_4 from shortwave infrared (SWIR, 2300–2389 nm) wavelengths. Because of its high spatial resolution and data quality, TROPOMI has, for example, shown to be able to observe local NO_2 emission sources such as power plants (Beirle et al., 2019), gas compressor stations (van der A et al., 2020) and cities (Lorente et al., 2019), detailed volcanic SO_2 plumes (Theys et al., 2019), and CH_4 leakage from oil/gas fields (Pandey et al., 2019; Varon et al., 2019; Schneising et al., 2020). Recently, NO_2 plumes from individual ships have been identified with TROPOMI in areas where the ocean sunglint enhances the signal-to-noise (Georgoulias et al., 2020).

The small pixel size of TROPOMI also causes cloud shadows to be detectable. Cloud shadow signatures can be found along cloud edges, manifested as pixels with smaller radiances than measured in their cloud-free neighborhood. Smaller measured radiances result in lower derived reflectance values, potentially affecting TROPOMI's air quality products. Cloud shadow effects on air quality data sets can only be studied, discarded and/or corrected if the cloud shadow contaminated pixels are identified. Individual shadow pixels may be identified manually in maps of TROPOMI data through visual inspection. However, for the automatic removal or correction of shadow contaminated data, and for the statistical analysis of shadow effects on large data sets, an automatic shadow detection is needed.

For satellite spectrometer measurements, cloud shadow detection is a new topic and will become more important with the increasing spatial resolution in future satellite spectrometer missions, such as Sentinel-5 (7.5×7.3 km^2) (Pérez Albiñana et al., 2017), CO2M ($< 2 \times 2$ km^2) (Sierk et al., 2021) and TANGO (300×300 m^2) (Landgraf et al., 2020). For high spatial resolution aerial and satellite imagers, shadow detection is not new. Shadows of buildings affect the applications of aerial images, such as

---

[1]The radiance co-addition time reduced from 1080 to 840 ms starting in orbit 9388. This resulted in a decrease of the minimal along-track sampling distance from 7 km at nadir to 5.5 km at nadir (see Sect. 14 of Ludewig et al., 2020).

urban change detection and traffic monitoring (see Adeline et al., 2013, and references therein). The screening of clouds and their shadows is an important step in the preprocessing of satellite imager data of for example Landsat and MODIS (see Zhu et al., 2018; Wang et al., 2019). Shadows degrade the quality of the images lowering the accuracy of their applications such as land cover classification and change detection (see e.g. Yan and Roy, 2020). If cloud shadows are not screened correctly, they may be confused with dark surface features such as, for example, water bodies affecting the remote sensing performance of flood detection (Li et al., 2013).

Several approaches have been followed by aerial and spaceborne imagers to detect cloud shadows. The main approaches can be categorized into geometry-based methods (Simpson and Stitt, 1998; Simpson et al., 2000; Hutchison et al., 2009) where the shadow location is computed with known or assumed parameters of the cloud shadow geometry, and spectral-based methods (see e.g. Ackerman et al., 1998) where the shadow is determined with spectral tests applied to the measured radiance. Often, a combination of those approaches is being used, first determining the potential cloud shadow locations with one of the two approaches and subsequently refining the shadows with the other approach (see e.g. Huang et al., 2010; Zhu and Woodcock, 2012; Sun et al., 2018). The spectral tests may consist of simple darkness thresholds, however dark surface features can easily incorrectly be interpreted as shadows. Luo et al. (2008) therefore presented a method to detect cloud shadows in MODIS images exploiting the ratio between the blue and NIR (or SWIR) spectral bands, arguing that shadows may appear more blue due to the lack of direct solar illumination. Luo et al. (2008) concluded that their method is problematic over water regions and wetlands, because the relatively dark spectra of water and shadows are difficult to distinguish. Additionally, the blueness of shadows may depend on the shadow geometry and cloud parameters such as thickness and height.

Unsupervised machine learning (clustering) techniques have been proposed for urban shadow detection in aerial images, but the spectral variability of the shadowed materials can complicate the choice of the number of classes (see the review of Adeline et al., 2013, and references therein). Because various cloud and land surface types may be mixed within individual pixels of satellite imagery, Bo et al. (2020) proposed a fuzzy clustering algorithm for cloud and cloud shadow detection in Landsat images, in which pixels can belong to multiple classes with associated weighting factors. Supervised machine learning techniques (neural networks and support vector machines) have been proposed for cloud shadow detection in satellite images also (see e.g. Hughes and Hayes, 2014; Ibrahim et al., 2021), but are generally computationally expensive, require large training data sets with classified shadows (which itself is the problem to be solved), and trained classifiers may not work for new scenes with different shadow patterns (Adeline et al., 2013; Zhu et al., 2018).

The most suitable approach for shadow detection for a satellite imager depends on the characteristics of the instrument and its host satellite. For example, the cloud and cloud shadow detection algorithm Fmask for Landsat 4-7, introduced by Zhu and Woodcock (2012), uses for its geometry-based part the thermal band (10.4 to 12.5 μm) measuring the cloud's brightness temperature. Assuming a constant lapse rate, Fmask computes the cloud top height and projection of the cloud shadow onto the surface. For imagers that do not have a thermal band, a range of potential cloud heights can be assumed (see Zhu et al., 2015, for the application of Fmask to Landsat-8) or the approach can be limited to spectral tests only. Parmes et al. (2017) proposed a cloud and cloud shadow detection method for Suomi NPP VIIRS only based on spectral tests avoiding the usage of a thermal band, and suggested that the method could therefore also work for Sentinel-2 which does not have a thermal band.

However, the accuracy of their shadow detection was low (36.1%), with a false alarm rate of 82.7%. Goodwin et al. (2013), Zhu and Woodcock (2014), Candra et al. (2016) and Candra et al. (2019) chose to perform spectral tests based on the reflectance differences with cloud-free historical reference images, for Landsat cloud shadow detection. Such multi-temporal shadow detection approaches generally enhance the shadow detection performance (Zhu et al., 2018), but require the availability of cloud-free seasonally dependent reference images which may be challenging for satellites with long revisit periods.

In this paper we present the Detection AlgoRithm for CLOud Shadows (DARCLOS), a fast cloud shadow detection algorithm for TROPOMI and the first cloud shadow detection algorithm for a spaceborne spectrometer. DARCLOS starts with a geometry-based computation of potential shadow locations, using the cloud fraction, cloud height, viewing and illumination geometries, and surface height stored in the already available TROPOMI NO$_2$ product and cloud product FRESCO. Climatological cloud-free surface albedo reference data is available for TROPOMI and is used to perform spectral tests refining the shadows. The spectral tests are only based on the darkness of shadows relative to the reference data. This means that no assumptions are made about the color of cloud shadows. As TROPOMI is a spectrometer, DARCLOS exploits the spectra of TROPOMI by using the wavelength for shadow detection where the surface reflectance is strongest, independent of surface classification. We validate the PCSF and ACSF with true color images of Suomi NPP VIIRS which orbits in close proximity to TROPOMI. Because geometrical shadow extents may be wavelength dependent, DARCLOS also outputs a wavelength dependent cloud shadow flag for the wavelengths at which TROPOMI's air quality products are retrieved. Such a cloud shadow detection at the precise wavelengths of TROPOMI's air quality products is unique for DARCLOS and cannot be done with data from an imager.

This paper is structured as follows. In Sect. 2, we explain the method to detect cloud shadows in TROPOMI data. In Sect. 3, we show the results of the cloud shadow detection algorithm with three case studies. In Sect. 4, the validation results are presented. In Sect. 5, we discuss the limits of the algorithm and raise several points of attention for future applications. In Sect. 6, we summarize the results and state the most important conclusions of this paper.

2 Method

Here, we explain the method to detect cloud shadows in TROPOMI data. We first compute the potential cloud shadow flag (PCSF), explained in Sect. 2.1, and then compute the actual cloud shadow flag (ACSF), explained in Sect. 2.2. Figure 1 summarizes the inputs and outputs of DARCLOS. The PCSFs indicate the TROPOMI ground pixels that are potentially affected by cloud shadows based on a geometric consideration with safety margins. The ACSFs are a refinement of the PCSFs using spectral reflectance information of the PCSF pixels, and indicate the TROPOMI ground pixels that are confidently affected by cloud shadows. The PCSF can be used to exclude cloud shadow contamination from the TROPOMI Level 2 data, while the ACSF can be used to select pixels for the scientific analysis of cloud shadow effects. The spectral cloud shadow flag (SCSF) is a wavelength dependent alternative for the ACSF and will be explained in Sect. 5.
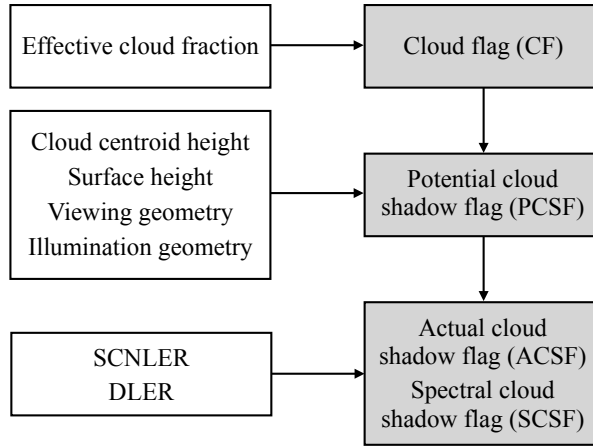
Figure 1. Summary of the inputs and outputs of DARCLOS. The white boxes describe the main input data and the grey boxes describe the calculated output products. SCNLER refers to the reflectivity of the scene (Sect. 2.2.1) and DLER refers to the climatological directionally dependent surface reflectivity (Sect. 2.2.2). More details are provided in the main text.

2.1 Potential cloud shadow flag (PCSF)

125 The PCSFs indicate the pixels that are potentially affected by cloud shadows. The PCSF is intended to be useful for filtering any cloud shadow contaminated TROPOMI data. Therefore, the number of false negative shadow detections in the PCSF should be minimized (see Sect. 4). Hence, the PCSF shadow is an overestimation of the true shadowed area.

The PCSF is computed in two steps. First, we compute the maximum potential geometric shadow extent from the cloud, with additional safety margins. Then, we flag the area between the cloud and the maximum potential shadow extent. Both steps

130 are explained in more detail below.

2.1.1 The maximum potential shadow extent

Figure 2 illustrates the cloud shadow geometry in the local reference frame at the Earth's surface. The reference frame is equivalent to the topocentric reference frame of TROPOMI (see Loots et al., 2017), except for the xy-plane which is now lifted in the zenith direction with the surface height h_{sfc} w.r.t. the WGS84 Earth reference ellipsoid. Here, the origin (point O) of

135 the reference frame is set at the center of a cloud pixel, which represents the projection of the cloud's centroid in the viewing direction onto the Earth's surface at geodetic latitude δ_{c} and longitude ϑ_{c}. The cloud pixels are the TROPOMI ground pixels with a raised cloud flag (CF) and are determined by an effective cloud fraction (the cloud fraction assuming a cloud albedo of 0.8) larger than 0.05. The effective cloud fraction was determined in the NO_2 spectral window and taken from the TROPOMI NO_2 data product (van Geffen et al., 2021). Angles θ_0 and θ are the solar and viewing zenith angles, respectively. Angles φ_0

140 and φ are the solar and viewing azimuth angles, respectively, measured positively clockwise from the North when looking in
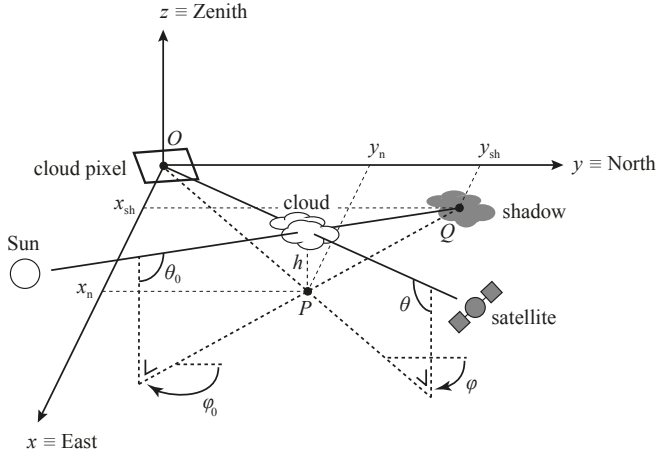
Figure 2. Sketch of the cloud shadow geometry in the local reference frame at the Earth's surface. The cloud as observed by the satellite is located at point O, resulting in a TROPOMI cloud pixel at O (indicated by the white quadrilateral), while the actual cloud is located at height h above point P. The shadow is located at point Q.
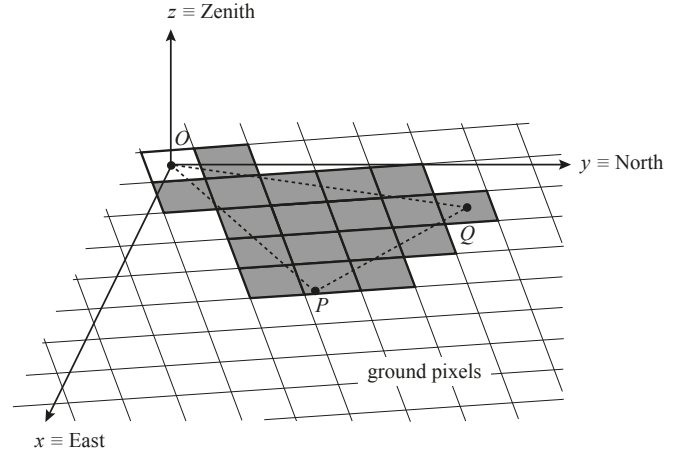
Figure 3. Sketch of the PCSF flagging of the TROPOMI ground pixels in the local reference frame at the Earth's surface. The PCSF pixels are indicated in grey and the cloud pixel is indicated by the white quadrilateral. Points O, P. and Q correspond to points O, P and Q in Fig. 2.

the nadir direction. The values for θ_0, θ, φ_0 and φ are provided in the TROPOMI data for the origin of the *unlifted* topocentric reference frame, i.e., when $h_{\text{sfc}} = 0$. In the problem of finding the cloud shadow belonging to the cloud pixel at the origin, we neglect variations of θ_0, θ, φ_0 and φ in the horizontal (x and y) and vertical (z) direction, and we assume that h_{sfc} is constant.

145   The location, dimensions and darkness of a cloud shadow cast on the Earth's surface and/or atmosphere below the cloud, as observed from space, may depend on (1) the cloud's location in 3-dimensional space, (2) the location of the underlying surface and/or atmosphere on which the shadow is cast in 3-dimensional space, (3) the horizontal and vertical extents of the cloud, (4) the optical thickness of the cloud, (5) the optical thickness of the atmospheric layers, (6) the illumination geometry (θ_0 and φ_0), and (7) the viewing geometry (θ and φ). Because in the first step of the PCSF determination we search for the maximum potential shadow extent, we assume an opaque cloud and neglect the optical thickness of the atmospheric layers, such that the

150   computed shadows are cast on the Earth's surface where the shadow separation from the cloud is largest.

In Fig. 2, the cloud is located at $(x_{\text{n}}, y_{\text{n}}, h)$. Point P at $(x_{\text{n}}, y_{\text{n}}, 0)$ is the nadir projection of the cloud's centroid onto the surface and h is the cloud height w.r.t. the surface, which can be computed as

$$h = (1 + C)\left(h_{\text{c}} - h_{\text{sfc}}\right). \tag{1}$$

In Eq. (1), h_{c} is the FRESCO cloud height (Koelemeijer et al., 2001; Wang et al., 2008), which is an approximation of the true

155   height of the cloud's centroid w.r.t. the WGS84 Earth reference ellipsoid. Because, for the PCSF, we search for the maximum potential shadow extent, we have introduced the safety margin C which increases the cloud height proportional to $h_{\text{c}} - h_{\text{sfc}}$.

We set $C = 0.5$, for which the number of false negative shadow detections (i.e. the omission error of the PCSF, see Sect. 4) resulting from underestimated maximum potential shadow extents converged to a minimum.

If we assume that the center of the cloud pixel is the projection of the cloud's centroid in the viewing direction onto the Earth's surface, x_n and y_n can be computed as (see also Luo et al., 2008):

$$x_n = h \cdot \tan\theta \sin\varphi, \tag{2}$$
$$y_n = h \cdot \tan\theta \cos\varphi. \tag{3}$$

The location of point Q in the cloud shadow on the Earth's surface, (x_{sh}, y_{sh}), then follows from:

$$x_{sh} = x_n - h \cdot \tan\theta_0 \sin\varphi_0, \tag{4}$$
$$y_{sh} = y_n - h \cdot \tan\theta_0 \cos\varphi_0. \tag{5}$$

Finding the geodetic latitude, δ_{sh}, and longitude, ϑ_{sh}, of Q is an example of the direct geodetic problem for which the solution involves an iterative procedure (Vincenty, 1975). However, because of the small distances in the cloud shadow geometry relative to the Earth's radii of curvature, δ_{sh} and ϑ_{sh} can accurately be approximated by differential northing and easting formulae:

$$\delta_{sh} \approx \delta_c + \frac{y_{sh}}{M + h_{sfc}}, \tag{6}$$
$$\vartheta_{sh} \approx \vartheta_c + \frac{x_{sh}}{(N + h_{sfc})\cos\delta_c}, \tag{7}$$

where M and N are the Earth's ellipsoidal meridian radius of curvature and radius of curvature in the prime vertical, respectively, which both vary with latitude δ_c (see e.g. Torge and Müller, 2012).

The center of the cloud pixel may not coincide with the projection of the cloud's centroid in the viewing direction onto the Earth's surface, as was assumed in Eqs. (2) and (3). This is particularly true, for example, when small clouds in the pixel are located near the pixel edges or corners, or when the edge of a large cloud deck traverses the pixel. Moreover, the actual projections of the unknown true horizontal and vertical cloud extents are located inside but near the edges of the cloud pixel.[2] Therefore, we repeat the computation of point Q four times, now placing the *corners* of the cloud pixel in the origin of the reference frame (not shown in Fig. 2).

2.1.2 Raising the PCSF

In the second step of the PCSF determination, we select the area in which PCSFs are to be raised, based on the calculated points P and Q. As illustrated in Fig. 3, we flag all the cloud-free ground pixels (i.e. for which no CF is raised) within or intersected by the triangle OPQ.

All cloud-free ground pixels intersected by line segment OQ are flagged for two reasons. First, OQ is the projection in the viewing direction onto the Earth's surface of a line segment, between the cloud's centroid and point Q, where the shadowed atmosphere is located (e.g., an optically thick atmosphere may lead to short shadows, cast on the atmospheric layers, projected

---

[2]An even larger horizontal or vertical cloud extent would be part of an adjacent cloud pixel.

onto the surface close to point O). Secondly, a possible overestimation of h implies an actual cloud's nadir projection closer to O (along line OP) which, with an unchanged illumination geometry, results in a shadow location between O and Q on line segment OQ.

All cloud-free ground pixels intersected by line segment PQ are flagged because the vertical cloud extent below the cloud's centroid is unknown. Although the vertical cloud extent of an isolated cloud may result in an adjacent cloud pixel, the vertical extent *below* the cloud's centroid may be invisible from space if neighboring clouds cover the volume below the cloud's centroid. For that reason, line segment PQ represents the potential shadow locations of a hypothetical cloud extending from the cloud's centroid to the surface.

All cloud-free ground pixels within or intersected by triangle OPQ are flagged, because combinations of the aforementioned situations may occur. For similar reasons as mentioned in Sect. 2.1.1, we repeat the flagging four times for the triangles OPQ where O is placed in the corners of the cloud pixel (not shown in Fig. 3).

2.2 Actual cloud shadow flag (ACSF)

In this section, the computation of the ACSF is explained. The ACSFs indicate the pixels that are confidently affected by cloud shadows. They are a subset of the PCSFs, and are intended to be useful for selecting pixels for the scientific analysis of cloud shadows. The number of false positive shadow detections in the ACSF should therefore be minimized (see Sect. 4).

The ACSF is determined in two steps. First, we apply a Rayleigh scattering correction to the measured reflectance at the top of the atmosphere for the PCSF pixels. Then, we compare the corrected reflectance to the expected surface reflectance from climatological observations by TROPOMI, revealing the actual shadowed pixels. This comparison is done at the wavelength where the surface reflectance is strongest. Both steps are explained in more detail below.

2.2.1 Lambertian-equivalent reflectivity of the scene (SCNLER)

The spectral Earth's reflectance at the top of the atmosphere (TOA) as measured by a satellite is defined as

$$R^{\text{meas}}(\mu, \mu_0, \varphi, \varphi_0, \lambda) = \frac{\pi I(\mu, \mu_0, \varphi, \varphi_0, \lambda)}{\mu_0 E_0(\lambda)}, \tag{8}$$

where I is the radiance reflected by the atmosphere-surface system in W m^{-2}sr^{-1}nm^{-1}, E_0 is the extraterrestrial solar irradiance perpendicular to the beam in W m^{-2}nm^{-1} and $\mu_0 = \cos\theta_0$. I and E_0 depend on wavelength λ in nm, and I additionally depends on $\mu = \cos\theta$, μ_0, φ and φ_0.

First, we calculate the albedo of the surface, A_s, needed to match a modeled TOA reflectance, R^{model}, to the measured TOA reflectance, R^{meas}. The model assumes a Lambertian (i.e., depolarizing and isotropic reflecting) surface below a cloud-free and aerosol-free atmosphere, such that the modeled TOA reflectance can be expressed as (Chandrasekhar, 1960):

$$R^{\text{model}}(\mu, \mu_0, \varphi - \varphi_0, \lambda) = R^0(\mu, \mu_0, \varphi - \varphi_0, \lambda) + \frac{A_s(\lambda)T(\mu, \mu_0, \lambda)}{1 - A_s(\lambda)s^*(\lambda)}. \tag{9}$$

The first term at the right-hand side of Eq. (9), R^0, is the so-called path reflectance, which is the modeled TOA reflectance of the atmosphere bounded below by a black surface. The second term is the modeled surface contribution to the TOA reflectance,

where A_s is the albedo of the Lambertian surface, T is the total transmittance of the atmosphere for illumination from above and below, and s^* is the spherical albedo of the atmosphere for illumination from below. Quantities R^0, T and s^* of the cloud-free and aerosol-free atmosphere-surface model were prepared with the 'Doubling-Adding KNMI' (DAK) radiative transfer code (de Haan et al., 1987; Stammes, 2001), version 3.2.0, taking into account single and multiple Rayleigh scattering of sunlight by molecules in a pseudo-spherical atmosphere, including polarization. Absorption by O_3, NO_2, O_2, H_2O and the O_2-O_2 collision complex was taken into account. For more details about the computation of the quantities in Eq. (9), we refer to Tilstra (2022).

The albedo A_s for which $R^{\mathrm{model}}(\lambda) = R^{\mathrm{meas}}(\lambda)$ holds is in this paper indicated by A_{scene}. The expression for A_{scene} follows from Eq. (9) (see e.g. Tilstra et al., 2017):

$$A_{\mathrm{scene}}(\lambda) = \frac{R^{\mathrm{meas}}(\lambda) - R^0(\lambda)}{T(\lambda) + s^*(\lambda)(R^{\mathrm{meas}}(\lambda) - R^0(\lambda))}, \tag{10}$$

where the notation for the dependency on μ, μ_0, φ and φ_0 is omitted. We compute A_{scene} for $\lambda = 402, 416, 425, 440, 463, 494, 670, 685, 696.97, 712.7, 747, 758$ and 772 nm, and co-register the results at NIR wavelengths to the Level 2 UVIS ground pixel grid. The values of A_{scene} can be interpreted as the TOA reflectances of the scene corrected for molecular Rayleigh scattering. They are in fact scene albedos, because they include non-Lambertian surface, aerosol, cloud and shadow effects. Therefore, in what follows, we refer to A_{scene} as the Lambertian-equivalent reflectivity of the scene (SCNLER). Only in the absence of non-Lambertian effects, A_{scene} is independent of μ, μ_0, φ and φ_0 and approximates the true surface albedo.

2.2.2 Directionally dependent Lambertian-equivalent reflectivity (DLER) climatology

In the second step of the ACSF determination, the SCNLER of the PCSF pixels is compared to climatological observations at the same coordinates and time of the year. For the climatological observations, we use the directionally dependent Lambertian-equivalent reflectivity (DLER) data[3] version 0.6 generated with TROPOMI observations of the SCNLER since the start of TROPOMI's operational phase in May 2018. The DLER is available on a global $0.125°$ by $0.125°$ resolution latitude-longitude grid for each calendar month at 21 one-nm wide wavelength bins between 328 and 2314 nm (Tilstra, 2022). We linearly interpolate the DLER data to the TROPOMI Level 2 UVIS ground pixel grid and measurement times. Unless stated otherwise, the wavelength bins we use are centered at 402, 416, 425, 440, 463, 494, 670, 685, 696.97, 712.7, 747, 758 and 772 nm.

In the DLER algorithm, an initial cloud screening was performed on the basis of NPP-VIIRS cloud information. After that, the 10% lowest SCNLER measurements in the seasonal grid cell were used which serves as a second-stage cloud filter, and measurements containing aerosols were excluded (see Tilstra, 2022). The DLER can generally be considered shadow-free. The DLER takes into account the viewing zenith angle dependence of the SCNLER caused by non-Lambertian surface reflectance. The DLER is a more accurate estimate of the expected aerosol-, cloud- and shadow-free SCNLER than the traditionally used LER (without viewing zenith angle dependence). The viewing zenith angle dependence of the DLER is only taken into account over land surfaces. Over water surfaces, DLER = LER. For more details about the DLER theory, we refer to Tilstra et al. (2021).

---

[3]See https://www.temis.nl/surface/albedo/tropomi_ler.php, visited on 23 October 2021.

2.2.3 Raising the ACSF

In order to select the pixels for which an ACSF is to be raised, we define the SCNLER-DLER contrast parameter Γ:

$$\Gamma(\lambda) = \frac{A_{\text{scene}}(\lambda) - A_{\text{DLER}}(\lambda)}{A_{\text{DLER}}(\lambda)} \times 100\%. \tag{11}$$

The division by A_{DLER} (the value of the DLER) in Eq. (11) allows us to search for a A_{DLER}-independent ACSF threshold for Γ, that is, a single threshold that can be used for both dark and bright surface types. Because of the division by the DLER, Γ is more stable (i.e., less susceptible to potential offset errors in the DLER) when the DLER is high. For each PCSF pixel, we compute the wavelength for shadow detection, λ_{max}, at which the pixel's DLER is maximum:

$$\lambda_{\text{max}} = \underset{\lambda}{\text{argmax}} \; A_{\text{DLER}}(\lambda). \tag{12}$$

We raise an ACSF at PCSF pixels for which

$$\Gamma(\lambda_{\text{max}}) < q, \tag{13}$$

where q is the contrast threshold. We set $q = -15\%$, yielding the highest actual shadow detection score in the validation (see Sect. 4).

2.2.4 Rationale behind the SCNLER-DLER contrast parameter

Here, we demonstrate the behavior of the variables in Eqs. (11) to (13) which determine the SCNLER-DLER contrast parameter Γ with an example measurement. Figure 4 is a true color image made by the Visible Infrared Imager Radiometer Suite (VIIRS) instrument on board the Suomi National Polar-orbiting Partnership (NPP) satellite, on 3 August 2019 above Southern Chile and Argentina. Suomi NPP orbits in close proximity to Sentinel-5P: the measurement time intervals of TROPOMI and VIIRS were 19:00-19:01 UTC and 18:57-18:58 UTC, respectively. A specific land region (52.5°-50.5°S latitude and 71.5°-70°W longitude) and water region (53°-51.5°S latitude and 67.5°-66°W longitude) are indicated by red dashed boxes. The main surface types in those regions are steppe and ocean, respectively. Figures 5a and 5b show the spectral behavior of the mean and 1-σ of SCNLER measurements affected by shadow (A_{scene} shadow) and not affected by shadows (A_{scene} no shadow) of cloud-free TROPOMI pixels in the land and water region, respectively. We used the PCSF to remove shadow pixels and the ACSF to select shadow pixels. Also shown are the mean and 1-σ of the DLER interpolated on the TROPOMI Level 2 UVIS grid.

Figure 5a shows that over land (steppe), the DLER and the cloud- and shadow-free SCNLER follow a typical surface reflectivity spectrum for grasslands (cf. Fig. 7 of Tilstra et al., 2017): they increase with increasing wavelength, and include a subtle signature of the so-called 'red edge' (i.e., the sudden surface albedo increase at $\lambda \sim 700$ nm caused by vegetation). Over ocean, the DLER and cloud- and shadow-free SCNLER follow a typical surface reflectivity spectrum for ocean water: they increase with decreasing wavelength, and peak at $\lambda \sim 400$ nm where the peak significance depends on the water constituents (see also e.g. Morel and Maritorena, 2001). The mean value of A_{scene} affected by shadow is smaller than the DLER and
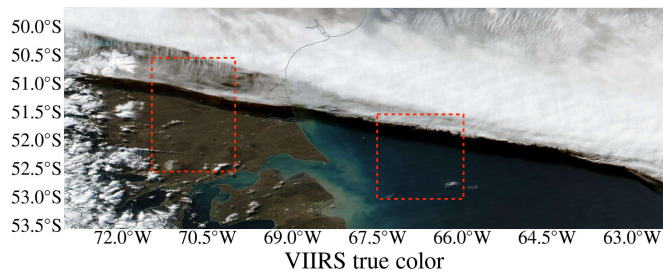
Figure 4. VIIRS-NPP true color image of Southern Chile and Argentina on 3 August 2019. The land and water regions belonging to the spectra of Fig. 5 are indicated by red dashed boxes.
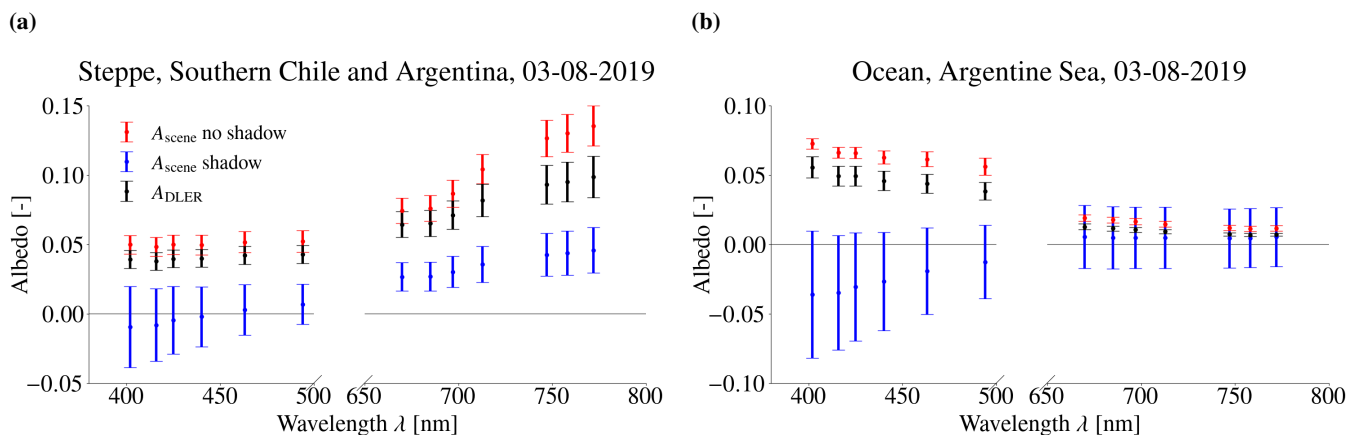
Figure 5. Spectra of the mean and 1-σ of the Lambertian-equivalent scene reflectivity (SCNLER) measured by TROPOMI at Southern Chile and Argentina on 3 August 2019, for the steppe region within $52.5°$-$50.5°$S latitude and $71.5°$-$70°$W longitude (Fig. 5a) and for the ocean region within $53°$-$51.5°$S latitude and $67.5°$-$66°$W longitude (Fig. 5b). Here, all measurements are cloud-free (i.e., without CF). The measurements affected by shadow (i.e., with ACSF) are presented in blue, and the shadow-free measurements (i.e., without PCSF) are presented in red. The additional black spectra are of the mean and 1-σ of the directionally dependent climatological Lambertian-equivalent reflectivity (DLER) at the TROPOMI ground pixels in the particular regions.

cloud- and shadow-free A_scene at all wavelengths, for both the land and water region. The shadow signature in the difference $A_\mathrm{scene} - A_\mathrm{DLER}$ is most evident at the wavelength where the DLER is highest. The Rayleigh scattering correction results in negative A_scene for part of the shadowed pixels. Above land, a slight increase of the shadowed A_scene can still be observed with increasing wavelength, but above ocean, the water albedo increase in the UV cannot be observed anymore. Note that the mean DLER is consistently smaller than the mean cloud- and shadow-free SCNLER measured at all wavelengths, which is expected since the DLER at a certain location was generated with the 10% lowest SCNLER values at that location.

Figure 6a shows λ_max on the TROPOMI Level 2 UVIS ground pixel grid for this measurement example. As expected from Fig. 5, $\lambda_\mathrm{max} = 772$ nm for the majority of the land covered pixels and $\lambda_\mathrm{max} = 402$ nm for the majority of the water covered pixels. In shallow water regions near the coast line, however, $\lambda_\mathrm{max} = 494$ nm, while in some land coast regions we find
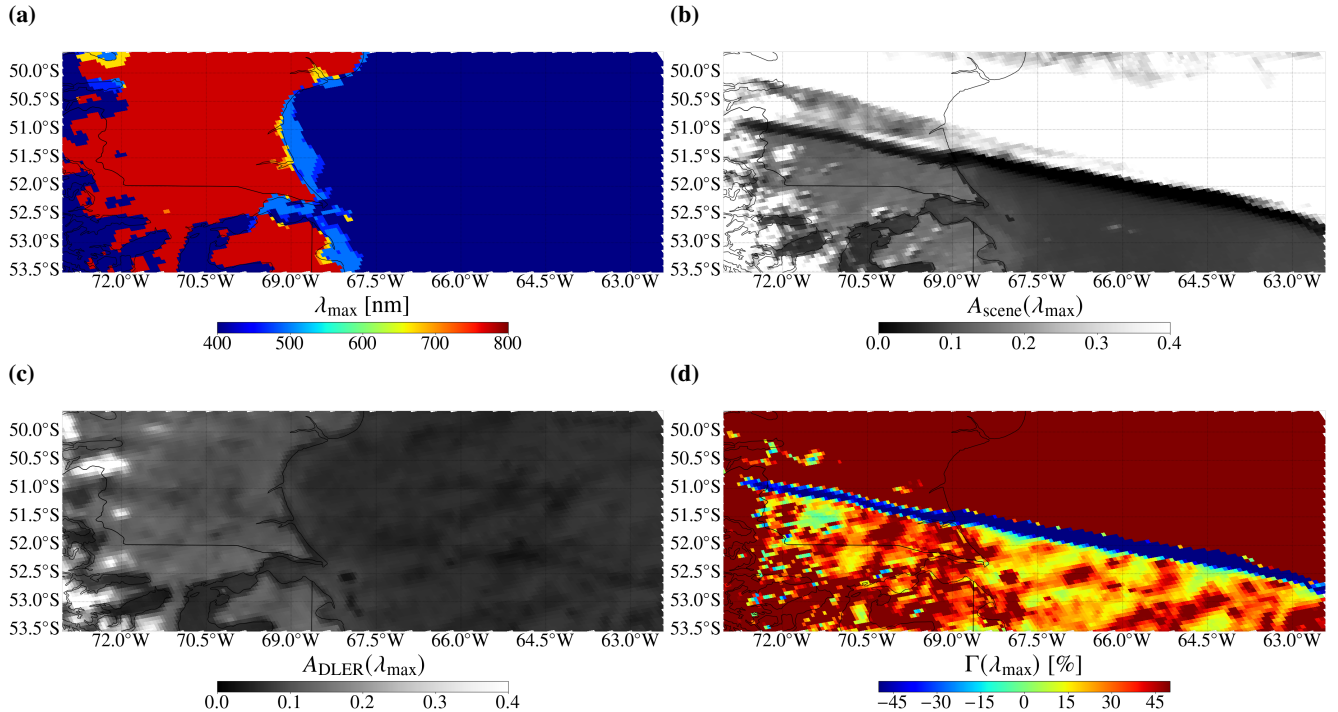
Figure 6. The wavelength at which DLER is maximum λ_{max} (Fig. 6a), the SCNLER at λ_{max} (Fig. 6b), the DLER at λ_{max} (Fig. 6c), and contrast parameter Γ at λ_{max} (Fig. 6d), for Southern Chile and Argentina on 3 August 2019.

$\lambda_{\mathrm{max}} = 670$ nm. Indeed, employing λ_{max}, the usage of surface type classification flags is avoided (see Romahn et al., 2021, for an example of surface type classification flags usage). That is, λ_{max} does not rely upon assumptions made in a surface type classification product, and will also give the most suitable wavelength for shadow detection when mixed and/or rare surface types are present within the pixel.

Figures 6b, 6c and 6d show A_{scene}, A_{DLER} and Γ, respectively, at λ_{max}. Cloud- and shadow-free pixels yield $\Gamma(\lambda_{\mathrm{max}}) \sim 0\%$ or slightly positive (up to $\sim 50\%$), because the DLER is generated with the 10% lowest SCNLER values in the particular calendar month that passed an aerosol- and cloud screening. The clouds at latitudes larger than $52.5°$ increase A_{scene} significantly relative to A_{DLER}, which results in $\Gamma(\lambda_{\mathrm{max}}) > 50\%$. Pixels affected by true shadows show a significantly decreased A_{scene} relative to A_{DLER}, which is most apparent for the elongated cloud shadow along the edge of the cloud deck.

3   Results

Here, we discuss the potential and actual cloud shadow flag results for three case studies with different cloud and surface types: the cloud deck example above steppe and ocean surfaces introduced in Sect. 2.2.4 (Sect. 3.1), an example with patchy clouds above grass and forest surfaces (Sect. 3.2) and an example of a relatively large area above the Sahara desert containing thin cirrus clouds (Sect. 3.3).
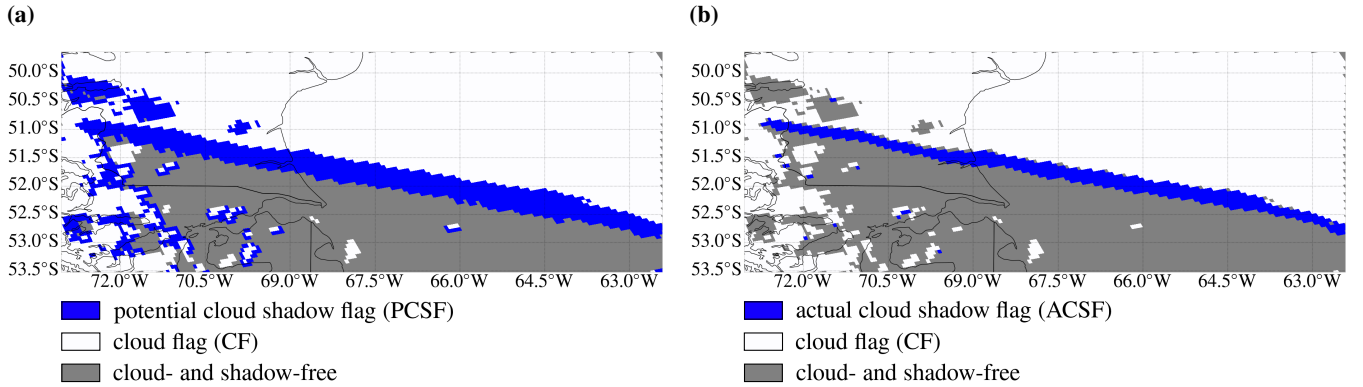
Figure 7. The TROPOMI Level 2 UVIS ground pixels for Southern Chile and Argentina on 3 August 2019 with raised PCSFs (Fig. 7a) and with raised ACSFs (Fig. 7b), indicated in blue. The white pixels are cloud pixels and grey pixels do not contain a raised cloud or shadow flag.

3.1 Southern Chile and Argentina, 3 August 2019

Figures 7a and 7b show (in blue) the TROPOMI Level 2 UVIS ground pixels with raised PCSFs and ACSFs, respectively, for the cloud shadow example on 3 August 2019 at Southern Chile and Argentina.

Figure 7a shows that the PCSFs indicate the presence of an elongated cloud shadow southward of the edge of the cloud deck longitudinally traversing the scene from $\sim 51°$S to $\sim 52.5°$S latitude. The southward shadow is expected because in this example the Sun is located in the Northwest (φ_0 ranges from -29.3° in the West to -41.7° in the East). The Sun is located relatively low in the sky because of the local winter season (θ_0 ranges from 72.2° in the Northwest to 79.7° in the Southeast), which is geometrically beneficial for the existence of long shadows (see Eq. (5)). The latitudinal extent of the elongated shadow is relatively large compared to the shadows of the isolated small clouds found at latitudes southward of $51.5°$S. This variation of shadow extent can be explained by the difference in cloud height: $h \sim 15$ km for the cloud deck, while $h \sim 1$ km for the isolated small clouds. The cloud deck shadow extent is larger than expected from visual inspection of the true color image (Fig. 4), which is caused by the cloud height safety margin C that we included in Eq. (1).

Figure 7b shows that the latitudinal extent of the cloud deck shadow detected with the ACSF is a more realistic approximation of the latitudinal cloud deck shadow extent observed in the true color image of Fig. 4. Only a few shadows of small isolated clouds are detected by the ACSF. Note that part of the small isolated clouds are in fact false positive cloud detections in the cloud product caused by bright surfaces. This can readily be concluded by comparing Fig. 7b to Fig. 4. For example, the water constituents along the coast between 53°S and 53.5°S latitude, but also the snowy mountains westward of 71°W, are falsely interpreted as clouds. These false cloud shadow detections in the PCSF are correctly filtered out by the threshold for $\Gamma(\lambda_{\mathrm{max}})$ (Eq. (13)), and are therefore not part of the ACSF. Indeed, the performance of the shadow detection algorithm depends on the quality of the input cloud and DLER products. The gaps in the cloud deck between $51°$S and $50°$S are caused by undefined cloud fractions in the cloud product, but again, the false PCSF shadow detections within those gaps are (except for 2 pixels) correctly removed from the ACSF.
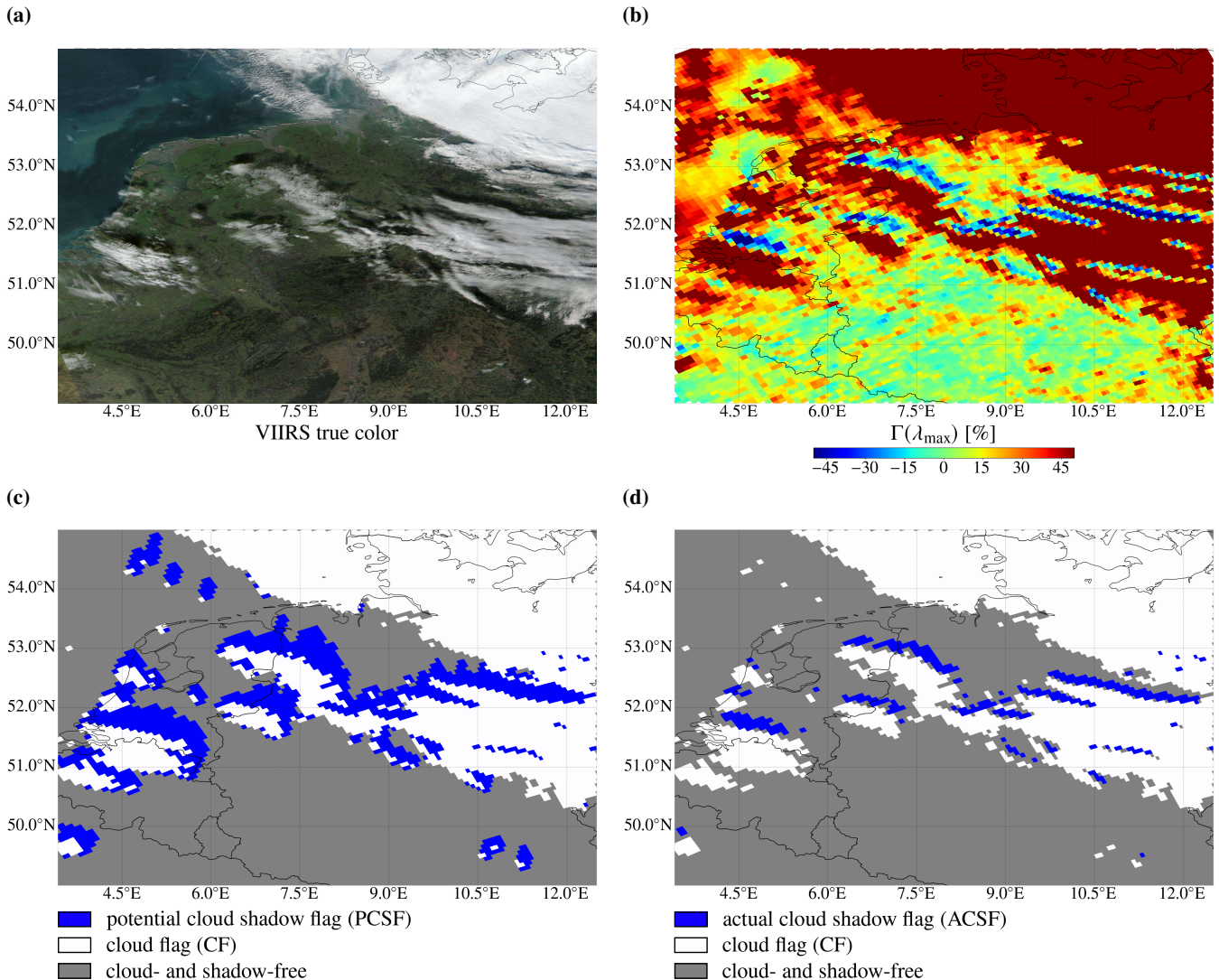
Figure 8. VIIRS-NPP true color image (Fig. 8a), SCNLER-DLER contrast parameter Γ at $\lambda_{\max}$ measured by TROPOMI (Fig. 8b), TROPOMI Level 2 UVIS ground pixels with raised PCSFs (Fig. 8c), and with raised ACSFs (Fig. 8d), for the Netherlands and Germany on 18 November 2018. In Figs. 8c and 8d, white pixels are cloud pixels and grey pixels do not contain a raised cloud or shadow flag.

3.2 The Netherlands and Germany, 18 November 2018

Figures 8a and 8c show the true color image and the TROPOMI Level 2 UVIS ground pixels with raised PCSFs, respectively,
for an example on 18 November 2018 above the Netherlands and Germany. TROPOMI orbits northwestward, and the viewing
geometry is southwestward: θ ranges from 8.8° in the Northeast to 54.3° in the Southwest. The Sun is located in the South (φ_0

ranges from -180.0° in the West to -165.7° in the East) and the solar zenith angle θ_0 ranges from 65.8° in the South to 76.8° in the North.

With the PCSF, long potential cloud shadows are found extending towards the Northeast. Here, all clouds that produce
330   shadows are relatively high ($h \sim 10$ km or higher). Note that at the location of the small isolated clouds above the sea at $\sim$ 54°N latitude and 4.5-6°E longitude, the Sun is almost directly located in the South. The eastward component of the potential shadow at these longitudes is caused by the parallax effect (cf. Fig. 2): the southwestward looking instrument projects the cloud as a cloud pixel onto the surface southwestward from the cloud's actual nadir location. Although the path from the cloud's nadir location to the actual shadow is strictly northward, the path from the cloud *pixel* to the actual shadow is northeastward.

335   The majority of the cloud shadows in this example are found above land surface. The main land surface types in this part of Europe are grassland and forest, with in general a higher vegetation density than for the steppe land in the example shown in Sect. 3.1. Consequently, the red edge is more pronounced in this example resulting in a stronger surface reflectance in the near-infrared. Hence, we find that λ_{max} = 772 nm for all pixels over land. The relatively high surface reflectance in the near-infrared results in a clear shadow signature in $\Gamma(\lambda_{max})$ (see Fig. 8b): in the cloud- and shadow-free regions $\Gamma(\lambda_{max})$ equals 0 or
340   is slightly positive, while strong negative $\Gamma(\lambda_{max})$ values are confined to cloud shadows (cf. Fig. 8a).

Figure 8d shows the TROPOMI Level 2 UVIS ground pixels with raised PCSFs for this example. Comparing the shadows detected with the ACSF to the true color image of Fig. 8a shows that ACSF shadows are detected where they can be expected. The small high isolated clouds above the sea do not produce dark enough shadows for an ACSF to be raised, similar to the small high isolated clouds above land at $\sim$49.5°N latitude and $\sim$10.5°-11°E longitude.

345   **3.3   Sahara desert, 18 January 2021**

Figure 9 is equivalent to Fig. 8, but then for an example above the Sahara desert on 18 January 2021. The area of this example covers most of the orbit swath of TROPOMI traveling north-northwestward: θ ranges from 66.5° in the West-southwest to -58.1° in the East-northeast. Although the latitudes in this example are relatively small, the local winter season causes the Sun not to be located directly overhead (θ_0 ranges from 28.4° in the South to 59.3° in the North, and φ_0 ranges from -178.7° in the
350   West to -140.3° in the East).

With the PCSF, northward shadows of longitudinally elongated cirrostratus clouds between 25°N and 28°N latitude, and of cirrocumulus clouds between 13°N and 22.5°N latitude, are detected. For both cloud types, $h > 10$ km. The vertical location of the detected foggy patch at 15°-17.5°N latitude and 14°-19°E longitude is just above the surface, hence the absence of the potential shadow (see Fig. 9c). This example is a clear demonstration of the parallax effect: on the west side of the area,
355   TROPOMI looks westward projecting the clouds as cloud pixels onto the surface 'too far' westward, resulting in an *eastward* component of the potential shadow locations w.r.t. the cloud pixels. Similarly, on the east side of the area, TROPOMI looks eastward and potential shadows tend to be located *westward* of the cloud pixels.

With the ACSF, the detected shadows are a more accurate approximation of the shadows observed in the true color image (cf. Figs. 9d and 9a). The most distinctive shadow signature in the true color image, which is the northward shadow of the
360   longitudinally elongated cirrostratus cloud between 25°N and 27°N latitude, is indeed also detected by the ACSF. Although,
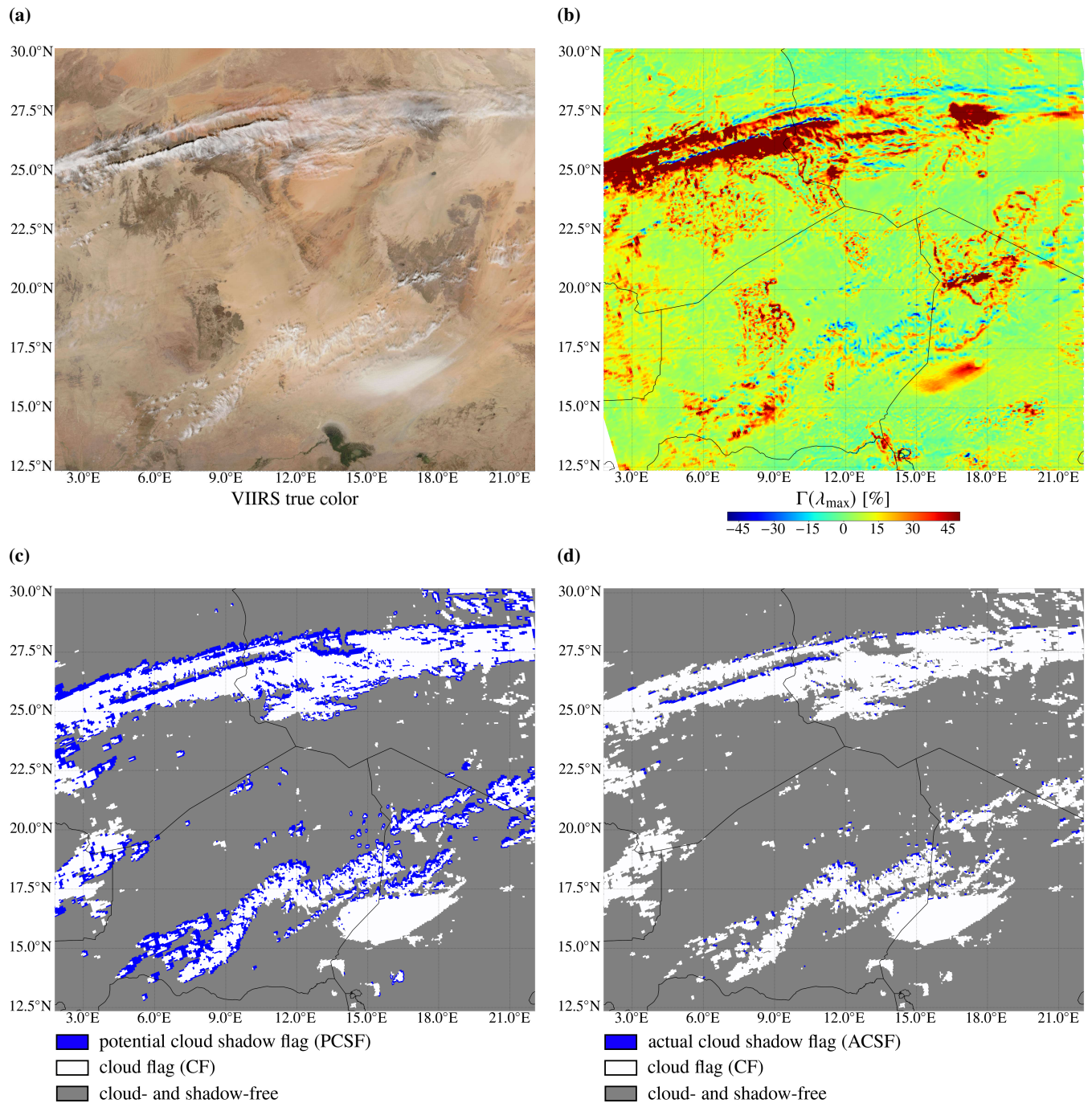
Figure 9. Similar to Fig. 8, but for the Sahara desert on 18 January 2021.

geometrically, many other clouds in this example are high enough to produce potential cloud shadows, some of those clouds are

too small and/or too thin to produce actual cloud shadows. This can be seen in Fig. 9b: for example, the cirrocumulus clouds near 13.5°N latitude and 4.5°E longitude are not able to decrease $\Gamma(\lambda_{max})$ significantly enough for an ACSF to be raised.

The spectral reflectance of desert surface does not contain a red edge, but is relatively strong already at $\lambda < 700$ nm and further increases with increasing wavelength (see e.g. Fig. 7 of Tilstra et al., 2017). We find that for almost all pixels in this example, $\lambda_{max} = 772$ nm. Comparing Fig. 9b with the false color image of Fig. 9a shows that strong negative $\Gamma(\lambda_{max})$ are strictly confined to cloud shadows (except for a few pixels near 12.7°N latitude and 17.8°E longitude). The cloud- and shadow-free area yield $\Gamma(\lambda_{max}) \sim 0$ or slightly positive. That is, dark surface features in the Sahara desert are not falsely detected as cloud shadows.

4 Validation

In this section, we validate DARCLOS by comparing the computed PCSFs and ACSFs to the shadows visually found at similar locations and time in VIIRS-NPP true color images. For the visual inspection of the true color images, we have developed an interactive Python tool which plots the TROPOMI Level 2 UVIS grid on top of the true color image. The software allows for the manual selection and de-selection of TROPOMI pixels containing VIIRS shadows by clicking on the image, after which the row and scanline numbers of the selected TROPOMI pixels are saved.

Figure 11a shows a VIIRS-NPP true color image of cloud shadows found at the Taklamakan desert at Xinjiang, China, on 22 December 2019. The red lines represent the TROPOMI Level 2 UVIS grid, and the blue crosses indicate the TROPOMI pixels with a raised ACSF. If, also, a VIIRS shadow is visually found at the TROPOMI pixel with a raised shadow flag, we speak of a true positive (TP) shadow detection. Similarly, we register the false positive (FP), false negative (FN), and true negative (TN) shadow detections (see Fig. 10).

The overestimation of the VIIRS shadow by DARCLOS can be expressed by the commission error, ϵ_C (see also e.g. Candra et al., 2016):

$$\epsilon_C = \frac{N_{FP}}{N_{TP} + N_{FP}}, \qquad (14)$$

	VIIRS shadow	VIIRS no shadow
TROPOMI shadow	True positive (TP)	False positive (FP)
TROPOMI no shadow	False negative (FN)	True negative (TN)

Figure 10. Confusion matrix of the shadow detection on the TROPOMI Level 2 UVIS grid. TROPOMI shadows are detected with the PCSF or ACSF of DARCLOS. VIIRS shadows are manually determined by visual inspection of VIIRS true color images.
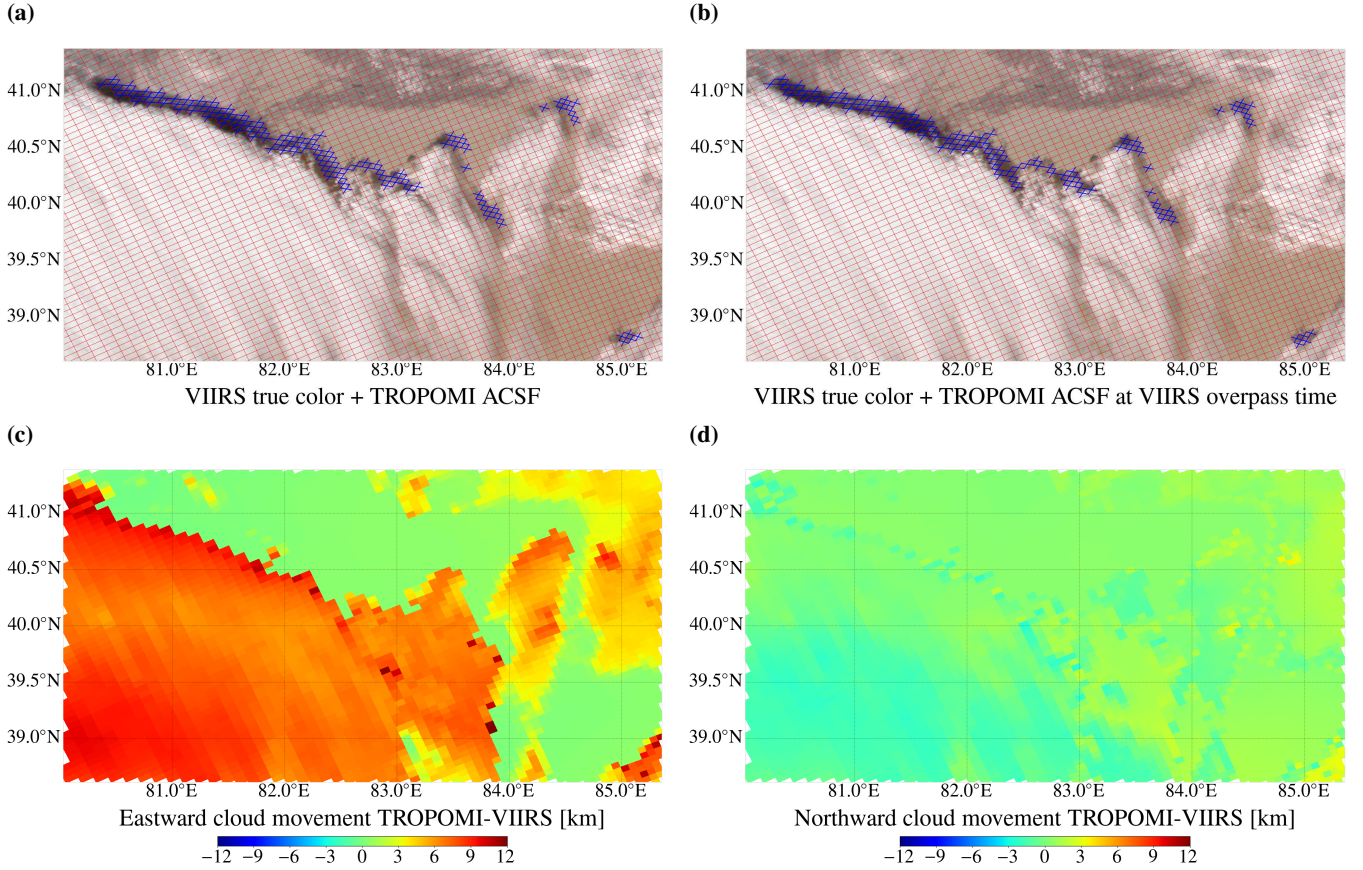
Figure 11. VIIRS-NPP true color image of the Taklamakan desert at Xinjiang, China, 22 December 2019, with the TROPOMI Level 2 UVIS grid plotted on top (in red) and the detected ACSF by DARCLOS (blue crosses), uncorrected (Fig. 11a) and at the VIIRS measurement times (Fig. 11b). Figures 11c and 11d show, respectively, the eastward and northward atmospheric movement at the cloud height during the TROPOMI-VIIRS measurement time difference, computed using ERA5 reanalysis wind data.

where N_{FP} and N_{FN} are the number of false positive detections and the number of false negative detections, respectively. The underestimation of the VIIRS shadow by DARCLOS can be expressed by the omission error, ϵ_O:

$$\epsilon_O = \frac{N_{FN}}{N_{TP} + N_{FN}}, \tag{15}$$

where N_{FN} are the number of false negative detections. For the definition of the VIIRS shadows, we distinguish between TROPOMI pixels that are totally shadowed (with geometrical shadow fractions $\gtrsim 0.75$), and partly shadowed (with geometrical shadow fractions $\gtrsim 0$ and $\lesssim 0.75$). For the computation of ϵ_O, we use only the totally shadowed pixels, while for the computation of ϵ_C, we use both the totally and partly shadowed pixels. That is, we consider the underestimation of the totally shadowed pixels, and the overestimation of the totally and partly shadowed pixels, to be erroneous. The overall performance of the algorithm can be assessed with the F_1 score which combines ϵ_C and ϵ_O as follows (see e.g. Fernández et al., 2018):

Example	Coordinates	Date	Orbit	Omission error PCSF	Commission error PCSF	Omission error ACSF	Commission error ACSF	F_1 score ACSF
Southern Chile and Argentina	53.528 - 49.626 °S 73.047 - 62.418 °W	03-08-2019	9355	**0.05**	0.48	0.10	0.01	**0.94**
The Netherlands and Germany	49.004 - 54.991 °N 3.4119 - 12.5062 °E	18-11-2018	5690	**0.06**	0.52	0.16	0.04	**0.90**
Sahara desert, North Africa	24.802 - 27.400 °N 3.506 - 12.011 °E	18-01-2021	16927	**0.14**	0.70	0.18	0.13	**0.84**
Taklamakan desert, China	36.500 - 43.000 °N 76.000 - 88.000 °E	22-12-2019	11348	**0.02**	0.77	0.08	0.02	**0.95**
The Netherlands, Belgium and Luxembourg	48.995 - 55.004 °N 2.000 - 8.000 °E	09-10-2018	5123	**0.05**	0.61	0.20	0.07	**0.86**
Taklamakan desert, China	37.006 - 42.005 °N 80.005 - 88.007 °E	21-12-2020	16527	**0.10**	0.51	0.13	0.11	**0.88**

Table 1. Results of the validation of the PCSF and ACSF by inspection of VIIRS-NPP true color images. The final results are shown in bold.

$$F_1 = \frac{2(1 - \epsilon_{\mathrm{C}})(1 - \epsilon_{\mathrm{O}})}{(2 - \epsilon_{\mathrm{C}} - \epsilon_{\mathrm{O}})}. \tag{16}$$

In the hypothetical case of a perfect shadow detection, we would obtain $\epsilon_{\mathrm{O}} = 0$, $\epsilon_{\mathrm{C}} = 0$ and F_1 score = 1. For the ACSF in a slightly larger area than shown in Fig. 11a (36.5 - 43.0 °N, 76.0 - 88.0 °E), the results are $\epsilon_{\mathrm{O}} = 0.27$, $\epsilon_{\mathrm{C}} = 0.21$ and F_1 score = 0.76.

It can be observed that the TROPOMI pixels with a raised ACSF in Fig. 11a are consistently located slightly eastwards of the shadows found in the VIIRS true color image. The eastward shift can be explained by the motion of the clouds during the measurement time difference of TROPOMI and VIIRS. In the example of Fig. 11, the VIIRS measurements were on average taken 4.33 minutes ahead of the TROPOMI measurements, with a 1-σ of 0.07 minutes[4]. We interpolate ERA5 data (Hersbach et al., 2018) of hourly eastward and northward wind speed components, provided at 37 vertical pressure levels on a 0.25° by 0.25° latitude-longitude grid, onto the FRESCO cloud pressure on the TROPOMI Level 2 UVIS grid (i.e., *without* manually raising the cloud height such as in Eq. (1)). The cloud deck in the South-west in Fig. 11 is relatively high (the cloud pressure is

---

[4]TROPOMI-VIIRS measurement times differences were taken from the S5P-NPP cloud product, which is the cloud product of VIIRS regridded to the TROPOMI Level 2 grid (see Siddans, 2016).

~ 400 hPa), where eastward wind speeds between 20 and 40 m/s are found. The eastward and northward cloud displacements are shown in Fig. 11c and 11d, respectively. The cloud displacements from ~ 6 to ~ 9 km are significant enough to shift some clouds, and hence some cloud shadows, at least one TROPOMI ground pixel in the eastward direction.[5]

In Fig. 11b we have corrected the locations of the TROPOMI cloud and cloud shadow pixels for the eastward and northward movement of the clouds during the TROPOMI-VIIRS measurement time difference. Note the much better agreement between the ACSF and the VIIRS shadows compared to Fig. 11a. Indeed, using the corrected ACSF, the errors decreased and the F_1 score increased: $\epsilon_O = 0.08$, $\epsilon_C = 0.02$ and F_1 score = 0.95. It should be noted that the validation may suffer from an imperfect correction of the cloud movement during the TROPOMI-VIIRS measurement time difference, because the cloud evolution is ignored and because of the relatively coarse resolution of the wind product. Therefore, we expect the true shadow detection performance at the TROPOMI measurement time to be even better than the performance presented with this validation.

The last 3 columns of Table 1 show the results for ϵ_O, ϵ_C and the F_1 score of the ACSF for the three examples discussed in this paper, and three additional examples (on the 22nd of December 2019, on the 9th of October 2018, and on the 21st of December 2020) not shown in this paper. The F_1 score is 0.84 or higher for all examples. The F_1 score is highest (0.94 and 0.95 respectively) for Southern Chile and Argentina, 3 August 2019, and for the Taklamakan desert, 22 December 2019. The shadows in those examples are caused by relatively large and thick cloud decks, and are therefore relatively distinctive. The examples with the lowest F_1 scores (0.84 and 0.86 respectively) are the Sahara desert, 18 January 2021, and The Netherlands, Belgium and Luxembourg, 9 October 2018. The shadows in those examples are caused by relatively thin and small clouds, and are therefore relatively subtle. Subtle shadows lead to less distinctive shadow signatures in Γ, leading to more false negative shadow detections and a higher ϵ_O of the ACSF. Also, thin and/or small clouds are sometimes not detected by the cloud product because the cloud fraction is too low to raise a CF, resulting in false negative PCSFs and ACSFs. Moreover, we speculate that thinner and/or smaller clouds are more likely to appear and disappear during the TROPOMI-VIIRS measurement time difference, complicating the cloud movement correction and validation of these examples.

The fourth and fifth column of Table 1 show ϵ_O and ϵ_C, respectively, of the PCSF. The value of ϵ_C of the PCSF is higher than 0.48 and higher than that of the ACSF, since the shadow in the PCSF is, by definition, an overestimation of the actual shadow. Because the PCSF is intended to be useful for excluding any cloud shadow contamination from TROPOMI Level 2 data, ϵ_O of the PCSF should be minimized. The value of ϵ_O for all examples is 0.14 or lower. Also here, we attribute the nonzero ϵ_O to the imperfect correction of the cloud movement during the TROPOMI-VIIRS measurement time difference, and to thin and/or small clouds resulting in false negative CF. Again, the best performances are found for Southern Chile and Argentina, 3 August 2019, and for the Taklamakan desert, 22 December 2019, with an ϵ_O of 0.05 and 0.02, respectively.

In order to put the validation results in perspective, we note that the state-of-the art imager cloud and cloud shadow detection code Fmask version 4.0 (Qiu et al., 2019) reports shadow detection commission errors of 0.49 for Landsat 4-7 and 0.38 for

---

[5]It should be noted that the cloud movement during the TROPOMI-VIIRS measurement time difference implies that the cloud flags (retrieved at the TROPOMI measurement time) cannot be replaced in DARCLOS by cloud flags from the S5P-NPP cloud product (retrieved at the VIIRS measurement time). Moreover, Fig. 11 is a general warning for all applications of the S5P-NPP cloud product which require a spatial cloud precision of about the size of a TROPOMI ground pixel.

435 Landsat 8, and omission errors of 0.27 for Landsat 4-7 and 0.31 for Landsat 8. Using multi-temporal reference images of specific regions, Candra et al. (2019) achieved omission and commission errors ranging from 0.001 to 0.084 and 0 to 0.058, respectively, depending on the region. The PCSF omission errors and ACSF commission errors in Table 1 are lower than those of Fmask 4.0, and are of the same order of magnitude as those achieved by Candra et al. (2019). Of course, because of the much higher spatial resolution of Landsat than that of TROPOMI, the error values for Landsat actually refer to a much larger

440 number of pixels.

5 Discussion

Here, we discuss some limitations and points of attention for the usage of the DARCLOS cloud shadow flags. Also, we point out the possible spectral dependence of cloud shadow extents, and present the (unvalidated) spectral cloud shadow flag as an auxiliary product of DARCLOS.

445 ### 5.1 Limitations of the ACSF and PCSF

The PCSF depends on the CF which is determined by the effective cloud fraction. As discussed in Section 3.1, false negative cloud detections in the CF can result in falsely detected gaps in cloud decks, resulting in false positive PCSFs inside the gaps (Fig. 7a). Note that false negative cloud detections in the CF can also result in false *negative* shadow detections in the PCSF and ACSF, since there is no shadow to be detected in the absence of a cloud detection. The surface albedo input for the effective

450 cloud fraction calculation in the NO_2 product is the LER climatology made by the Ozone Monitoring Instrument (OMI) at 440 nm available at a $0.5° \times 0.5°$ latitude-longitude grid (Kleipool et al., 2008). With a future implementation of the TROPOMI DLER climatology, which uses a $0.125° \times 0.125°$ latitude-longitude grid instead (see Sect. 2.2.2), in the effective cloud fraction algorithm, the accuracy of the CF, PCSF and ACSF is expected to further increase.

DARCLOS has not been tested at regions covered by ice and/or snow, nor at sunglint geometries over ocean. In these

455 circumstances, the performance of the current effective cloud fraction is limited, often resulting in false positive CFs. For the ACSF, we have discarded the cloud pixels (and corresponding shadows) that contain a raised sunglint flag and/or snow/ice flag. For the PCSF, these pixels are not discarded, such that they are removed from the data when the PCSF and CF are used together to both remove cloud and cloud shadow contaminations. With future potential improvements of FRESCO above glint and snow/ice regions, DARCLOS could be tested above glint and snow/ice regions. Then, the DLER for snow/ice conditions (see

460 Tilstra, 2022) should be employed in DARCLOS, and possibly an ocean surface reflectance calculation can help distinguishing between clouds and then glint.

The performance of the ACSF depends on the quality of the DLER climatology. Although the DLER takes into account monthly surface reflectivity changes throughout the year, temporary deviations from this climatology (e.g., agricultural land usage changes, forest fires, precipitation, flooding and snow cover) are measured by the SCNLER, and may affect Γ and

465 possibly the ACSF. In addition, the spatial resolution of the DLER of $0.125° \times 0.125°$ is somewhat coarser than the spatial resolution of the TROPOMI Level 2 UVIS grid at which the SCNLER is measured. Dark small-scale surface features not
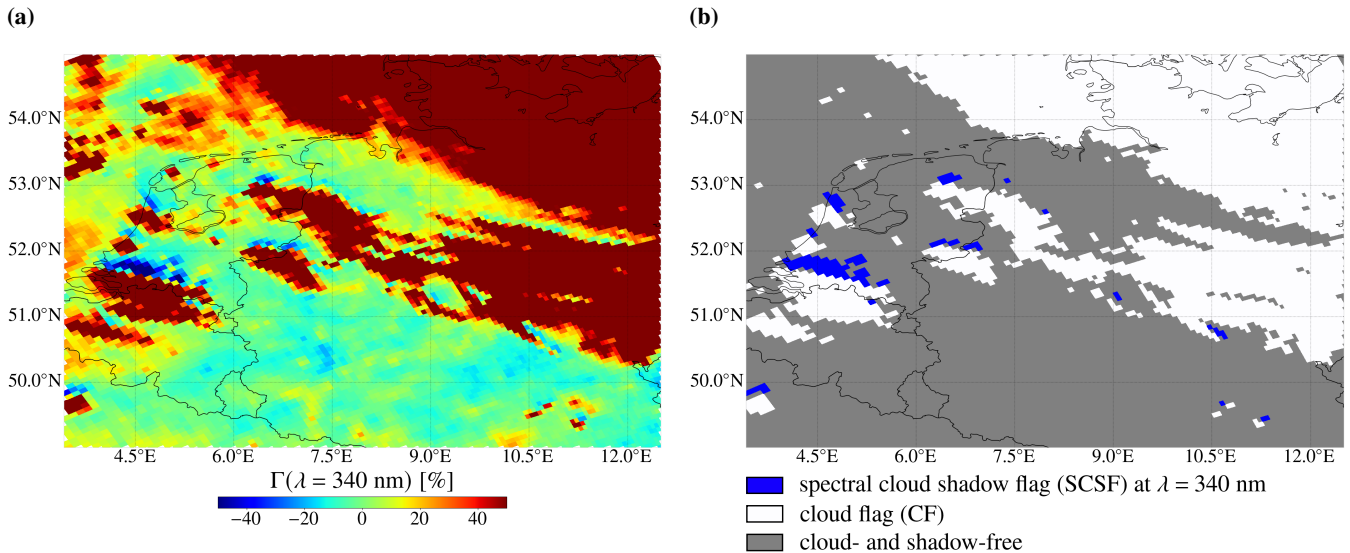
Figure 12. SCNLER-DLER contrast parameter Γ at $\lambda = 340$ nm measured by TROPOMI (Fig. 12a) and TROPOMI Level 2 UVIS ground pixels with raised SCSFs at $\lambda = 340$ nm (Fig. 12b), for the Netherlands and Germany on 18 November 2018. In Fig. 12b, white pixels are cloud pixels and grey pixels do not contain a raised cloud or shadow flag.

captured by the DLER may, theoretically, give too low Γ and may result in false positive ACSF. In the examples treated in this paper, however, dark small-scale forest (Sect. 3.2) and desert (Sect. 3.3) features did not convincingly deteriorate the ACSF performance.

470   Both the irradiance and radiance measurements by TROPOMI have degraded during its operational lifetime. The irradiance measurements are known to degrade faster than the radiance measurements (and most significantly at the shortest wavelengths), leading to an increasing derived reflectance over time (Tilstra et al., 2020; Ludewig et al., 2020). Since the release of the version 2.0.0 TROPOMI level 1b processor on 5 July 2021, the irradiance degradation is being corrected. The thresholds used in this paper for clouds and cloud shadows, which were set at an effective cloud fraction of 0.05 and $\Gamma = -15\%$ respectively, may

475   have to be adjusted for the corrected data.

5.2   Spectral cloud shadow flag (SCSF)

In Sect. 4, the ACSF has been validated by visual inspection of true color images of the VIIRS instrument. Hence, the shadows found with the ACSF can be interpreted as the shadows that could be observed from space by the human eye. We find, however, a significant wavelength dependency of the contrast parameter Γ in the UV part of the spectrum. For example, Fig. 12a shows

480   Γ at 340 nm for the example above the Netherlands and Germany on 18 November 2018. Comparing to Γ at λ_{max} (Fig. 8b), where $\lambda_{max} = 772$ nm over land, the negative Γ related to cloud shadows between 52°-53°N latitude and 9°-12°E longitude have disappeared. Also, the locations of some pixels with significant negative Γ have changed. Although these shadows have not been validated (they could possibly not be observed by the human eye) or could be a result of noisy Γ in dark scenes

(cf. Eq. (11)), they may be relevant for studying shadow effects on TROPOMI air quality products retrieved at particular UV wavelengths, such as the Absorbing Aerosol Index (AAI) at $\lambda = 340$ nm and $\lambda = 380$ nm (see de Graaf et al., 2005; Stein Zweers et al., 2018; Kooreman et al., 2020) or the NO_2 column at $\lambda = 440$ nm (see van Geffen et al., 2021). Therefore, DARCLOS also outputs the spectral cloud shadow flag (SCSF), which is raised at PCSF pixels for which:

$$\Gamma(\lambda) < q, \tag{17}$$

where q is again set at -15%. Contrary to the ACSF (Eq. 13), the SCSF is by definition wavelength dependent. The SCSF is computed at 328, 335, 340, 354, 367, 380, 388, 402, 416, 425, 440, 463, 494 nm.

Figure 12b shows the SCSF at $\lambda = 340$ nm for the example above the Netherlands and Germany on 18 November 2018. Comparing to Fig. 8d shows that part of the shadow flags has disappeared or has changed location. For example, the cloud shadow detected with the SCSF at $\sim 49.5°$N latitude and $\sim 11.3°$E longitude has shifted closer to the cloud as compared to the corresponding ACSF shadow. We speculate that the wavelength dependence of shadow locations in the UV can be explained by the wavelength dependence of the molecular scattering optical thickness of the atmosphere: at shorter wavelengths, the molecular scattering optical thickness is higher such that higher atmospheric layers are probed from space, decreasing the observed shadow extents with TROPOMI. The explanation and validation of the wavelength dependence of observed cloud shadow extents in the UV is subject to future research.

6   Summary and conclusions

In this paper, we have demonstrated DARCLOS, a cloud shadow detection algorithm for TROPOMI. DARCLOS provides a potential cloud shadow flag (PCSF) based on geometric variables stored in TROPOMI Level 2 data, and an actual cloud shadow flag (ACSF) based on the contrast of the measured scene reflectivity with the climatological surface reflectivity. For each TROPOMI pixel, this contrast is computed at the wavelength where the DLER is largest. The ACSFs are a subset of the PCSFs.

Three case studies with different spectral surface albedo and cloud types have been discussed in detail. We have shown that the PCSF vastly overestimates the shadows observed in true color images of the VIIRS-NPP instrument, as expected. The shadows detected with the ACSF are better approximations of these true shadows, but may miss some shadows that are produced by thin and/or small clouds. We showed that the shadow signatures in the contrast between the scene reflectivity and the climatological surface reflectivity can, for almost all pixels, only be attributed to cloud shadows. That is, dark surface features are not falsely detected as cloud shadows in the ACSF.

The PCSF and ACSF are validated by visual inspection of true color images made by the VIIRS-NPP instrument, for in total six cases. We found that the cloud motion during the measurement time difference between TROPOMI and VIIRS complicates this validation strategy. We showed that a cloud movement correction using the wind speed vectors at the cloud height significantly improves the validation results. The best detection scores were achieved for the cases with relatively thick and horizontally large cloud decks (ACSF F_1 score ≥ 0.94 and PCSF omission error ≤ 0.05). After the cloud movement

correction, the validation may still suffer from cloud evolution and the relatively coarse resolution of the wind product. Hence, the true shadow detection performance at the TROPOMI measurement times may be expected to be even better than presented with the validation in this paper.

At UV wavelengths, we have found cloud shadow signatures at different locations than determined with the ACSF, poten-
520 tially indicating a wavelength dependence of cloud shadow extents. Because TROPOMI's air quality products are retrieved at specific wavelengths or wavelength ranges, DARCLOS also outputs the spectral cloud shadow flag (SCSF), which is a wavelength dependent alternative for the ACSF. Such a cloud shadow detection at the precise wavelengths of TROPOMI's air quality products is unique for DARCLOS and cannot be done with data from an imager.

The shadow flags of DARCLOS are planned for implementation in the TROPOMI L2 SCNLER product. DARCLOS is, to
525 the best of our knowledge, the first cloud shadow detection algorithm for a spaceborne spectrometer instrument. In principle, DARCLOS can also be used for other spectrometer instruments than TROPOMI which have a spatial resolution high enough to observe cloud shadows. An effective cloud fraction and climatological surface albedo are prerequisites for DARCLOS, and should therefore be available at the ground pixel grid of the instrument. It should be noted that, when computing the ACSF using UVIS and NIR wavelengths from different detectors, a co-registration of the SCNLER measurements from one detector
530 ground pixel grid to the other has to be performed. Ideally, true color images are available of the scenes with approximately the same measurement times, in order to validate the PCSF and ACSF by visual inspection and to optimize the cloud and cloud shadow thresholds.

We conclude that the PCSF can be used to remove cloud shadow contaminated pixels from TROPOMI Level 2 UVIS data, and that the ACSF can be used to select pixels for further analysis of cloud shadow effects. If both cloud and cloud shadow
535 effects are to be removed, the PCSF and CF can be used together. Also, the ACSF can be used to demonstrate and/or count the true shadows that would be observed from space by the human eye. However, at UV wavelengths, we have found indications of the wavelength dependence of cloud shadow signatures, and a spectrally dependent cloud shadow flag such as the SCSF could possibly be more suitable when selecting shadow pixels in air quality products retrieved at UV wavelengths. Further research is needed to explain and validate the spectral dependence of these cloud shadow signatures. The detection of shadows with the
540 ACSF and SCSF allows users to perform this analysis, and is a first step towards the understanding and correction of cloud shadow effects on satellite spectrometer air quality measurements.

Author contributions. V.T. did all computations and wrote the manuscript. P.W. weekly commented on the intermediate results and guided V.T. to focus on the most relevant aspects. L.G.T. provided the SCNLER algorithm and commented on intermediate results. All authors read the manuscript, provided feedback that led to improvements and were involved in the selection of the results presented in this paper.

545 *Competing interests.* The authors declare that they have no conflict of interest.

Acknowledgements. This work is part of the research programme User Support Programme Space Research (GO) with project number ALWGO.2018.016, which is (partly) financed by the Dutch Research Council (NWO).

References

Ackerman, S. A., Strabala, K. I., Menzel, W. P., Frey, R. A., Moeller, C. C., and Gumley, L. E.: Discriminating clear sky from clouds with MODIS, Journal of Geophysical Research, 103, 32,141–32,157, https://doi.org/10.1029/1998JD200032, 1998.

Adeline, K. R. M., Chen, M., Briottet, X., Pang, S. K., and Paparoditis, N.: Shadow detection in very high spatial resolution aerial images: A comparative study, ISPRS Journal of Photogrammetry and Remote Sensing, 80, 21–38, https://doi.org/10.1016/j.isprsjprs.2013.02.003, 2013.

Beirle, S., Borger, C., Dörner, S., Li, A., Hu, Z., Liu, F., Wang, Y., and Wagner, T.: Pinpointing nitrogen oxide emissions from space, Science Advances, 5, eaax9800, https://doi.org/10.1126/sciadv.aax9800, 2019.

Bo, P., Fenzhen, S., and Yunshan, M.: A Cloud and Cloud Shadow Detection Method Based on Fuzzy c-Means Algorithm, IEEE Journal of Selected Topics in Applied Earth Observations and Remote Sensing, 13, 1714–1727, https://doi.org/10.1109/JSTARS.2020.2987844, 2020.

Bovensmann, H., Burrows, J. P., Buchwitz, M., Frerick, J., Noël, S., Rozanov, V. V., Chance, K. V., and Goede, A. P. H.: SCIA-MACHY: Mission Objectives and Measurement Modes, Journal of Atmospheric Sciences, 56, 127–150, https://doi.org/10.1175/1520-0469(1999)056<0127:SMOAMM>2.0.CO;2, 1999.

Burrows, J. P., Weber, M., Buchwitz, M., Rozanov, V., Ladstätter-Weißenmayer, A., Richter, A., Debeek, R., Hoogen, R., Bramstedt, K., Eichmann, K.-U., Eisinger, M., and Perner, D.: The Global Ozone Monitoring Experiment (GOME): Mission Concept and First Scientific Results., Journal of Atmospheric Sciences, 56, 151–175, https://doi.org/10.1175/1520-0469(1999)056<0151:TGOMEG>2.0.CO;2, 1999.

Candra, D. S., Phinn, S., and Scarth, P.: Cloud and Cloud Shadow Masking Using Multi-Temporal Cloud Masking Algorithm in Tropical Environmental, ISPRS - International Archives of the Photogrammetry, Remote Sensing and Spatial Information Sciences, 49B2, 95–100, https://doi.org/10.5194/isprs-archives-XLI-B2-95-2016, 2016.

Candra, D. S., Phinn, S., and Scarth, P.: Automated Cloud and Cloud-Shadow Masking for Landsat 8 Using Multitemporal Images in a Variety of Environments, Remote Sensing, 11, 2060, https://doi.org/10.3390/rs11172060, 2019.

Chandrasekhar, S.: Radiative transfer, Dover Publications, New York, 1960.

de Graaf, M., Stammes, P., Torres, O., and Koelemeijer, R. B. A.: Absorbing Aerosol Index: Sensitivity analysis, application to GOME and comparison with TOMS, Journal of Geophysical Research (Atmospheres), 110, D01201, https://doi.org/10.1029/2004JD005178, 2005.

de Haan, J. F., Bosma, P. B., and Hovenier, J. W.: The adding method for multiple scattering calculations of polarized light, Astronomy & Astrophysics, 183, 371–391, 1987.

Fernández, A., García, S., Galar, M., Prati, R., Krawczyk, B., and Herrera, F.: Learning from Imbalanced Data Sets, Springer International Publishing, Springer Nature Switzerland AG, Cham, Switzerland, https://doi.org/10.1007/978-3-319-98074-4, 2018.

Georgoulias, A. K., Boersma, K. F., van Vliet, J., Zhang, X., van der A, R., Zanis, P., and de Laat, J.: Detection of NO_2 pollution plumes from individual ships with the TROPOMI/S5P satellite sensor, Environmental Research Letters, 15, 124037, https://doi.org/10.1088/1748-9326/abc445, 2020.

Goodwin, N. R., Collett, L. J., Denham, R. J., Flood, N., and Tindall, D.: Cloud and cloud shadow screening across Queensland, Australia: An automated method for Landsat TM/ETM+ time series, Remote Sensing of Environment, 134, 50–65, https://doi.org/10.1016/j.rse.2013.02.019, 2013.

Heath, D. F., Krueger, A. J., Roeder, H. A., and Henderson, B. D.: The solar backscatter ultraviolet and total ozone mapping spectrometer (SBUV/TOMS) for Nimbus G., Optical Engineering, 14, 323–331, https://doi.org/10.1117/12.7971839, 1975.

585   Hersbach, H., Bell, B., Berrisford, P., Biavati, G., Horányi, A., Muñoz Sabater, J., Nicolas, J., Peubey, C., Radu, R., Rozum, I., Schepers, D., Simmons, A., Soci, C., Dee, D., and Thépaut, J.-N.: ERA5 hourly data on pressure levels from 1979 to present., Copernicus Climate Change Service (C3S) Climate Data Store (CDS). (Accessed on 12-Oct-2021), https://doi.org/10.24381/cds.bd0915c6, 2018.

Huang, C., Thomas, N., Goward, S. N., Masek, J. G., Zhu, Z., Townshend, J. R. G., and Vogelmann, J. E.: Automated masking of cloud and cloud shadow for forest change analysis using Landsat images, International Journal of Remote Sensing, 31, 5449–5464, 590   https://doi.org/10.1080/01431160903369642, 2010.

Hughes, M. and Hayes, D.: Automated Detection of Cloud and Cloud Shadow in Single-Date Landsat Imagery Using Neural Networks and Spatial Post-Processing, Remote Sensing, 6, 4907–4926, https://doi.org/10.3390/rs6064907, 2014.

Hutchison, K. D., Mahoney, R. L., Vermote, E. F., Kopp, T. J., Jackson, J. M., Sei, A., and Iisager, B. D.: A Geometry-Based Approach to Identifying Cloud Shadows in the VIIRS Cloud Mask Algorithm for NPOESS, Journal of Atmospheric and Oceanic Technology, 26, 595   1388, https://doi.org/10.1175/2009JTECHA1198.1, 2009.

Ibrahim, E., Jiang, J., Lema, L., Barnabé, P., Giuliani, G., Lacroix, P., and Pirard, E.: Cloud and Cloud-Shadow Detection for Applications in Mapping Small-Scale Mining in Colombia Using Sentinel-2 Imagery, Remote Sensing, 13, 736, https://doi.org/10.3390/rs13040736, 2021.

Kleipool, Q. L., Dobber, M. R., de Haan, J. F., and Levelt, P. F.: Earth surface reflectance climatology from 3 years of OMI data, Journal of 600   Geophysical Research: Atmospheres, 113, https://doi.org/https://doi.org/10.1029/2008JD010290, 2008.

Koelemeijer, R. B. A., Stammes, P., Hovenier, J. W., and de Haan, J. F.: A fast method for retrieval of cloud parameters using oxygen A band measurements from the Global Ozone Monitoring Experiment, Journal of Geophysical Research, 106, 3475–3490, https://doi.org/10.1029/2000JD900657, 2001.

Kooreman, M. L., Stammes, P., Trees, V., Sneep, M., Tilstra, L. G., de Graaf, M., Stein Zweers, D. C., Wang, P., Tuinder, O. N. E., and 605   Veefkind, J. P.: Effects of clouds on the UV Absorbing Aerosol Index from TROPOMI, Atmospheric Measurement Techniques, 13, 6407–6426, https://doi.org/10.5194/amt-13-6407-2020, 2020.

Landgraf, J., Rusli, S., Cooney, R., Veefkind, P., Vemmix, T., de Groot, Z., Bell, A., Day, J., Leemhuis, A., and Sierk, B.: The TANGO mission: A satellite tandem to measure major sources of anthropogenic greenhouse gas emissions, in: EGU General Assembly Conference Abstracts, EGU General Assembly Conference Abstracts, p. 19643, 2020.

610   Levelt, P. F., van den Oord, G. H. J., Dobber, M. R., Malkki, A., Visser, H., de Vries, J., Stammes, P., Lundell, J. O. V., and Saari, H.: The Ozone Monitoring Instrument, IEEE Transactions on Geoscience and Remote Sensing, 44, 1093–1101, https://doi.org/10.1109/TGRS.2006.872333, 2006.

Li, S., Sun, D., and Yu, Y.: Automatic cloud-shadow removal from flood/standing water maps using MSG/SEVIRI imagery, International Journal of Remote Sensing, 34, 5487–5502, https://doi.org/10.1080/01431161.2013.792969, 2013.

615   Loots, E., Rozemeijer, N., Kleipool, Q., and Ludewig, A.: Algorithm theoretical basis document for the TROPOMI L01b data processor. Doc. No. S5P-KNMI-L01B-0009-SD, Issue 8.0.0, Royal Netherlands Meteorological Institute (KNMI), http://www.tropomi.eu/sites/default/files/files/S5P-KNMI-L01B-0009-SD-algorithm_theoretical_basis_document-8.0.0-20170601_0.pdf, [Online; accessed 13-August-2020], 2017.

Lorente, A., Boersma, K. F., Eskes, H. J., Veefkind, J. P., van Geffen, J. H. G. M., de Zeeuw, M. B., Denier van der Gon, H. A. C., Beirle, S., 620   and Krol, M. C.: Quantification of nitrogen oxides emissions from build-up of pollution over Paris with TROPOMI, Scientific Reports, 9, 20033, https://doi.org/10.1038/s41598-019-56428-5, 2019.

Ludewig, A., Kleipool, Q., Bartstra, R., Landzaat, R., Leloux, J., Loots, E., Meijering, P., van der Plas, E., Rozemeijer, N., Vonk, F., and Veefkind, P.: In-flight calibration results of the TROPOMI payload on board the Sentinel-5 Precursor satellite, Atmospheric Measurement Techniques, 13, 3561–3580, https://doi.org/https://doi.org/10.5194/amt-13-3561-2020, 2020.

625 Luo, Y., Trishchenko, A., and Khlopenkov, K.: Developing clear-sky, cloud and cloud shadow mask for producing clear-sky composites at 250-meter spatial resolution for the seven MODIS land bands over Canada and North America, Remote Sensing of Environment, 112, 4167–4185, https://doi.org/10.1016/j.rse.2008.06.010, 2008.

Morel, A. and Maritorena, S.: Bio-optical properties of oceanic waters: A reappraisal, Journal of Geophysics Research, 106, 7163–7180, https://doi.org/10.1029/2000JC000319, 2001.

630 Munro, R., Lang, R., Klaes, D., Poli, G., Retscher, C., Lindstrot, R., Huckle, R., Lacan, A., Grzegorski, M., Holdak, A., Kokhanovsky, A., Livschitz, J., and Eisinger, M.: The GOME-2 instrument on the Metop series of satellites: instrument design, calibration, and level 1 data processing - an overview, Atmospheric Measurement Techniques, 9, 1279–1301, https://doi.org/10.5194/amt-9-1279-2016, 2016.

Pandey, S., Gautam, R., Houweling, S., Denier van der Gon, H., Sadavarte, P., Borsdorff, T., Hasekamp, O., Landgraf, J., Tol, P., van Kempen, T., Hoogeveen, R., van Hees, R., Hamburg, S. P., Maasakkers, J. D., and Aben, I.: Satellite observations reveal ex-
635 treme methane leakage from a natural gas well blowout, Proceedings of the National Academy of Science, 116, 26 376–26 381, https://doi.org/10.1073/pnas.1908712116, 2019.

Parmes, E., Rauste, Y., Molinier, M., Andersson, Kaj, ., and Seitsonen, L.: Automatic Cloud and Shadow Detection in Optical Satellite Imagery Without Using Thermal Bands—Application to Suomi NPP VIIRS Images over Fennoscandia, Remote Sensing, 9, 806, https://doi.org/10.3390/rs9080806, 2017.

640 Pérez Albiñana, A., Erdmann, M., Wright, N., Martin, D., Melf, M., Bartsch, P., and Seefelder, W.: Sentinel-5: the new generation European operational atmospheric chemistry mission in polar orbit, in: Society of Photo-Optical Instrumentation Engineers (SPIE) Conference Series, vol. 10403 of *Society of Photo-Optical Instrumentation Engineers (SPIE) Conference Series*, p. 104030P, https://doi.org/10.1117/12.2268875, 2017.

Platt, U. and Stutz, J.: Differential Optical Absorption Spectroscopy, Springer Nature Switzerland AG, Cham, https://doi.org/10.1007/978-
645 3-540-75776-4, 2008.

Qiu, S., Zhu, Z., and He, B.: Fmask 4.0: Improved cloud and cloud shadow detection in Landsats 4-8 and Sentinel-2 imagery, Remote Sensing of Environment, 231, 111 205, https://doi.org/10.1016/j.rse.2019.05.024, 2019.

Romahn, F., Pedergnana, M., Loyola, D., Apituley, A., Sneep, M., and Veefkind, J. P.: Sentinel-5 precursor/TROPOMI 1 Level 2 Product User Manual O3 Tropospheric Column. Doc. No. S5P-L2-DLR-PUM-400C, Issue 02.03.00, Royal Netherlands Meteorological Institute
650 (KNMI), https://sentinel.esa.int/documents/247904/2474726/Sentinel-5P-Level-2-Product-User-Manual-Ozone-Tropospheric-Column, [Online; accessed 13-September-2021], 2021.

Schneising, O., Buchwitz, M., Reuter, M., Vanselow, S., Bovensmann, H., and Burrows, J. P.: Remote sensing of methane leakage from natural gas and petroleum systems revisited, Atmospheric Chemistry & Physics, 20, 9169–9182, https://doi.org/10.5194/acp-20-9169-2020, 2020.

655 Siddans, R.: S5P-NPP Cloud Processor ATBD. Doc. No. S5P-NPPC-RAL-ATBD-0001, Issue 1.0.0, RAL Space, https://sentinels.copernicus.eu/documents/247904/2476257/Sentinel-5P-NPP-ATBD-NPP-Clouds, [Online; accessed 10-November-2021], 2016.

Sierk, B., Fernandez, V., Bézy, J. L., Meijer, Y., Durand, Y., Bazalgette Courrèges-Lacoste, G., Pachot, C., Löscher, A., Nett, H., Minoglou, K., Boucher, L., Windpassinger, R., Pasquet, A., Serre, D., and te Hennepe, F.: The Copernicus CO2M mission for monitoring anthro-

pogenic carbon dioxide emissions from space, vol. 11852 of *Society of Photo-Optical Instrumentation Engineers (SPIE) Conference Series*, p. 118523M, https://doi.org/10.1117/12.2599613, 2021.

Simpson, J. J. and Stitt, J. R.: A procedure for the detection and removal of cloud shadow from AVHRR data over land, IEEE Transactions on Geoscience and Remote Sensing, 36, 880–897, https://doi.org/10.1109/36.673680, 1998.

Simpson, J. J., Jin, Z., and Stitt, J. R.: Cloud shadow detection under arbitrary viewing and illumination conditions, IEEE Trans. Geosci. Remote. Sens., 38, 972–976, 2000.

Stammes, P.: Spectral radiance modelling in the UV-visible range, IRS 2000: Current Problems in Atmospheric Radiation, edited by: Smith, W.L. and Timofeyev, Y.M., A. Deepak Publishing, Hampton, Virginia, pp. 385–388, 2001.

Stein Zweers, D., Apituley, A., and Veefkind, P.: Algorithm theoretical basis document for the TROPOMI UV Aerosol Index. Doc. No. S5P-KNMI-L2-0008-RP, Issue 1.1, Royal Netherlands Meteorological Institute (KNMI), http://www.tropomi.eu/sites/default/files/files/S5P-KNMI-L2-0008-RP-TROPOMI_ATBD_UVAI-1.1.0-20180615_signed.pdf, [Online; accessed 14-September-2020], 2018.

Sun, L., Liu, X., Yang, Y., Chen, T., Wang, Q., and Zhou, X.: A cloud shadow detection method combined with cloud height iteration and spectral analysis for Landsat 8 OLI data, ISPRS Journal of Photogrammetry and Remote Sensing, 138, 193–207, https://doi.org/10.1016/j.isprsjprs.2018.02.016, 2018.

Theys, N., Hedelt, P., De Smedt, I., Lerot, C., Yu, H., Vlietinck, J., Pedergnana, M., Arellano, S., Galle, B., Fernandez, D., Carlito, C. J. M., Barrington, C., Taisne, B., Delgado-Granados, H., Loyola, D., and Van Roozendael, M.: Global monitoring of volcanic SO_2 degassing with unprecedented resolution from TROPOMI onboard Sentinel-5 Precursor, Scientific Reports, 9, 2643, https://doi.org/10.1038/s41598-019-39279-y, 2019.

Tilstra, L. G.: TROPOMI ATBD of the directionally dependent surface Lambertian-equivalent reflectivity, KNMI Report S5P-KNMI-L3-0301-RP, Issue 1.2.0, https://www.temis.nl/surface/albedo/tropomi_ler.php, [Online; accessed 7-February-2022], 2022.

Tilstra, L. G., Tuinder, O. N. E., Wang, P., and Stammes, P.: Surface reflectivity climatologies from UV to NIR determined from Earth observations by GOME-2 and SCIAMACHY, Journal of Geophysical Research (Atmospheres), 122, 4084–4111, https://doi.org/10.1002/2016JD025940, 2017.

Tilstra, L. G., de Graaf, M., Wang, P., and Stammes, P.: In-orbit Earth reflectance validation of TROPOMI on board the Sentinel-5 Precursor satellite, Atmospheric Measurement Techniques, 13, 4479–4497, https://doi.org/10.5194/amt-13-4479-2020, 2020.

Tilstra, L. G., Tuinder, O. N. E., Wang, P., and Stammes, P.: Directionally dependent Lambertian-equivalent reflectivity (DLER) of the Earth's surface measured by the GOME-2 satellite instruments, Atmospheric Measurement Techniques, 14, 4219–4238, https://doi.org/10.5194/amt-14-4219-2021, 2021.

Torge, W. and Müller, J.: Geodesy, De Gruyter, Berlin, 2012.

van der A, R., de Laat, J., Eskes, H., and Ding, J.: Connecting the dots: NOx emissions along a West Siberian natural gas pipeline., Npj Climate and Atmospheric Science, 3, 16, https://doi.org/10.1038/s41612-020-0119-z, 2020.

van Geffen, J., Eskes, H., Boersma, K., and Veefkind, J.: TROPOMI ATBD of the total and tropospheric NO_2 data products. Doc. No. S5P-KNMI-L2-0005-RP, Issue 2.2.0, Royal Netherlands Meteorological Institute (KNMI), https://sentinel.esa.int/documents/247904/2476257/Sentinel-5P-TROPOMI-ATBD-NO2-data-products, [Online; accessed 18-August-2021], 2021.

Varon, D. J., McKeever, J., Jervis, D., Maasakkers, J. D., Pandey, S., Houweling, S., Aben, I., Scarpelli, T., and Jacob, D. J.: Satellite Discovery of Anomalously Large Methane Point Sources From Oil/Gas Production, Geophysical Research Letters, 46, 13,507–13,516, https://doi.org/10.1029/2019GL083798, 2019.

Veefkind, J. P., Aben, I., McMullan, K., Förster, H., de Vries, J., Otter, G., Claas, J., Eskes, H. J., de Haan, J. F., Kleipool, Q., van Weele, M., Hasekamp, O., Hoogeveen, R., Landgraf, J., Snel, R., Tol, P., Ingmann, P., Voors, R., Kruizinga, B., Vink, R., Visser, H., and Levelt, P. F.: TROPOMI on the ESA Sentinel-5 Precursor: A GMES mission for global observations of the atmospheric composition for climate, air quality and ozone layer applications, Remote Sensing of Environment, 120, 70–83, https://doi.org/10.1016/j.rse.2011.09.027, 2012.

700 Vincenty, T.: Direct and Inverse Solutions of Geodesics on the Ellipsoid with Applications of Nested Equations, Survey Review, 23, 88–93, https://doi.org/10.1179/sre.1975.23.176.88, 1975.

Wang, P., Stammes, P., van der A, R., Pinardi, G., and van Roozendael, M.: FRESCO+: an improved O_2 A-band cloud retrieval algorithm for tropospheric trace gas retrievals, Atmospheric Chemistry & Physics, 8, 6565–6576, 2008.

Wang, T., Shi, J., Letu, H., Ma, Y., Li, X., and Zheng, Y.: Detection and Removal of Clouds and Associated Shadows
705 in Satellite Imagery Based on Simulated Radiance Fields, Journal of Geophysical Research (Atmospheres), 124, 7207–7225, https://doi.org/10.1029/2018JD029960, 2019.

Yan, L. and Roy, D. P.: Spatially and temporally complete Landsat reflectance time series modelling: The fill-and-fit approach, Remote Sensing of Environment, 241, 111 718, https://doi.org/10.1016/j.rse.2020.111718, 2020.

Zhu, Z. and Woodcock, C. E.: Object-based cloud and cloud shadow detection in Landsat imagery, Remote Sensing of Environment, 118,
710 83–94, https://doi.org/10.1016/j.rse.2011.10.028, 2012.

Zhu, Z. and Woodcock, C. E.: Automated cloud, cloud shadow, and snow detection in multitemporal Landsat data: An algorithm designed specifically for monitoring land cover change, Remote Sensing of Environment, 152, 217–234, https://doi.org/10.1016/j.rse.2014.06.012, 2014.

Zhu, Z., Wang, S., and Woodcock, C. E.: Improvement and expansion of the Fmask algorithm: cloud, cloud shadow, and snow detection for
715 Landsats 4-7, 8, and Sentinel 2 images, Remote Sensing of Environment, 159, 269–277, https://doi.org/10.1016/j.rse.2014.12.014, 2015.

Zhu, Z., Qiu, S., He, B., and Deng, C.: Cloud and Cloud Shadow Detection for Landsat Images: The Fundamental Basis for Analyzing Landsat Time Series, Remote Sensing Time Series Image Processing, pp. 3–24, CRC Press, Boca Raton, https://doi.org/10.1201/9781315166636-1, 2018.